



UIT

THE ARCTIC
UNIVERSITY
OF NORWAY

Faculty of Science and Technology

Department of Geosciences

Geochemistry of rutile-bearing veins at Engerbøfjellet, Naustdal, Norway.

Kristoffer Grane

Master's thesis in [GEO-3900] - November 2018



Foreword

First, I would like to thank my supervisor Sabina Strmic Palinkas. For your patience and for taking your time to comment, discuss and answer my questions at all times. A special thanks also goes to my co-supervisor Steinar Kleppe and to Nordic Mining for allowing me to pursue my interest for the eclogite at Engebøfjellet. It was Steinars suggestion for further studies in his master thesis that led to this topic. Thank you for spending your time helping me with field work, drill core handling and for being available for discussions whenever I contacted you. Thank you also, Kai Neufeld, for helping me out with the analysis of thin sections in SEM, and for taking your time to get me up to speed using the SEM software.

Takk til alle som gjorde tida i Tromsø så fin.

Sist men ikkje minst, kjære Mamma og Pappa, mine søstre Maria og Solveig. Tusen takk for for den gode støtta.

Table of Contents

Foreword	
Abstract	3
1.1 Background	4
1.2 Thesis questions	5
2 Geological setting	6
2.1 Regional geology	6
2.2 Local geology	7
2.3 The Engebø Eclogite	8
2.4 The ore forming processes at the Engebøfjellet Eclogite	10
3 Methods	11
3.1 Field work	11
3.2 Optical microscopy	11
3.3 SEM / EDS	11
3.4 Fluid inclusions	12
3.5 Major and trace element analysis	13
3.6 La-Icp-MS	15
3.7 Stable isotopes analysis	16
4 Theoretical background	18
4.1 The formation of eclogites	18
4.2 Mobility and behaviour of trace elements in hydrothermal conditions	19
4.2.1 Solubility in hydrothermal systems	19
4.3 Fluid inclusions	21
4.4 Fluid inclusion microthermometric measurement and analysis	23
4.4.1 Recording data	24
4.4.2 The NaCl-H ₂ O System	27
4.4.3 The CO ₂ -NaCl-H ₂ O system	27
4.4.4 Calculating salinity, density and the isochore	28
5 Results	30
5.1 Field observations and sample overview	30
5.2 Eclogite matrix	35
5.2.1 Eclogite petrography	35
5.2.2 Major element composition	38
5.2.3 Trace element composition	39
5.2.4 Spot analysis of rutile as inclusions within garnet	42
5.2.5 Spot analysis of rutile and ilmenite in the eclogite matrix	43
5.2.6 Spot analysis of garnet and omphacite in ferro and leuco eclogite	44

5.3	Eclogite veins	46
5.3.1	Vein petrography.....	46
5.3.2	Carbonate in veins.....	46
5.3.3	Omphacite in veins.....	47
5.3.4	Rutile	49
5.3.5	Garnet.....	49
5.3.6	Pyrite.....	50
5.3.7	Ilmenite.....	50
5.3.8	Symplectite.....	51
5.4	Trace element composition of vein minerals.	52
5.4.1	Rutile and ilmenite trace element composition	52
5.4.2	Trace element composition of carbonate.	54
5.5	Stable isotopes.....	54
5.6	Fluid inclusions	55
5.6.1	Fluid salinity.....	57
5.6.2	Fluid inclusion isochores.....	58
6	Discussion	59
6.1	Geochemistry.	59
6.2	Trace element behaviour in texturally different rutile	61
6.3	Fluid characteristics.....	64
6.4	Conditions of titanium solubility.....	67
6.5	Source of fluids	68
6.6	Suggestion for a model of rutile precipitation in eclogite veins.	70
7	Suggestions for further studies.	71
8	Conclusion.....	71
9	References	72
	Appendix	76
	Fluid inclusion measurements.....	76

Abstract

The Engebøfjellet eclogite, located in Naustdal, Norway, contain quartz veins with large rutile (TiO₂) phenocrystals. Trace element composition of rutile deposited in veins and in the eclogite matrix was analysed with the use of LA-ICP-MS. The Nb content decrease with increasing V in the rutile, and contents of these elements vary depending on depositional environment. One quartz vein associated with rutile deposition and one carbonate vein was analyzed for fluid inclusion characteristics. These inclusions show fluid salinity ranging from 2-35 wt.% with an average of 16.3 wt.% NaCl equivalents. The fluid inclusion isochores was compared with previously published data of the exhumation path of the Engebøfjellet eclogite (Braathen & Erambert., 2014). A group of inclusions have the same slope, and almost cross deformation stages D3-D5 (garnet amphibolite – greenschist facies) – leading to the interpretation that fluids was entrapped along this path. A stable isotope analysis of $\delta^{13}\text{C}$ and $\delta^{18}\text{O}$ composition was performed on three carbonate veins. The carbonate samples plotted close to the field of primary igneous carbonatites (Taylor 1967). REE trace element fractionation patterns of the host rock eclogite resembles a normal mid ocean ridge basalt.

1.1 Background

Engebøfjellet have a rutile deposit hosted within its Eclogite lithology. The industrial mineral Rutile are used for a variety of purposes including a base for pigments and other consumer products (Meinhold 2010). At present Rutile (TiO_2) are not being mined from Eclogite. Today the main sources of rutile are mineral sands, or titano-magnetite magmatic ores such as the Tellnes deposit in Rogaland, Norway, and Lac Tio deposit in Canada. The magmatic deposits give ilmenite (FeTiO_3) as a feedstock, where rutile needs to be synthetically beneficiated to deliver rutile for the pigment market.

Rutile deposits hosted in eclogite could prove to be important sources of TiO_2 pigment in the future, as an alternative to the existing deposit types. If the Nordic Mining ASA rutile project in eclogite are proven successful, the demand for similar deposits could rise along with the general demand for TiO_2 .

Several companies including the current owners Nordic Mining ASA have been investigating the mining potential of the rutile deposit since it was discovered. Norges Geologiske Undersøkelse (NGU) (Korneliussen et al., 2000) have had considerable involvement in these studies. Other workers (Braathen et al., 2014) and (Kleppe 2013) have studied the structural and petrological evolution of the deposit.

The formation of the rutile in eclogite occurrences in the Sunnfjord region have been discussed by Korneliussen et al., (2000). It is currently believed that the rutile anomaly found in the Engebø eclogite can be traced back to elemental fractionation in the pre metamorphic, magmatic setting. Magmatic fractionation within the magma chamber that sourced the intrusion, or within the intrusion itself, caused deposition of heamo-ilmenite ores, rich in ilmenite and iron. Later, the gabbro intrusion suffered high grade metamorphism during plate collision. Under these conditions the gabbroic intrusion was metamorphosed into eclogite. Heamo ilmenite ores transformed by mineral reaction into Rutile and Garnet.

During uplift from the peak metamorphic conditions, the eclogite body was deformed and the eclogitic mineral assemblage was influenced by fluids that circulated within the ore body (Korneliussen et al., 2010). Transformation of rutile (TiO_2) to ilmenite (FeTiO_3) and titanite (CaTiSiO_5) are believed to have been influenced by the presence of fluids. The deformation and mineral reactions that occurred during uplift, shaped and formed the deposit we see today and are therefore a part of the ore forming processes at the Engebøfjellet.

Large (1-10cm) rutile phenocrystals deposited in quartz veins at Engebøfjellet was described by Kleppe, 2013. The presence of such veins at Engebøfjellet could indicate that the fluids have had chemical characteristics that allowed titanium mobility.

1.2 Thesis questions

This thesis aims to investigate the physical and chemical conditions of titanium mobilization in veins at the Engeøfjellet eclogite.

The goal for this thesis is to bring new or additional information to the following questions:

- Have rutile bearing veins been formed during the prograde or retrograde formation of the Engeøfjellet eclogite?
- At what pressure and temperatures was the rutile bearing veins deposited?
- What could have been the source of the rutile bearing fluid?.
- Are there any geochemical differences between rutile deposited in veins and rutile found in the rock matrix of the high and low grade eclogite?
- What are the geochemical differences between eclogites with high amounts of rutile and eclogites with low amounts of rutile?

This master thesis includes methods such as optical microscopy, scanning electron microscope, litho-geochemistry, La-Icp-MS, stable isotopes and fluid inclusions.

2 Geological setting

2.1 Regional geology

The western gneiss region (WGR) is located in the south western part of Norway, and extends from just north of Bergen to south of the Trondheim area (fig. 1). It is surrounded by allochthonous covers, emplaced during the Caledonian orogeny. The western gneiss complex (WGC) consists of crystalline rocks of granodioritic to tonalitic composition that were part of the western Baltic craton (Kylander-Clark et al., 2008). (The ages of the protoliths that make up the WGR vary, but are generally of Mesoproterozoic age (Braathen et al., 2014).

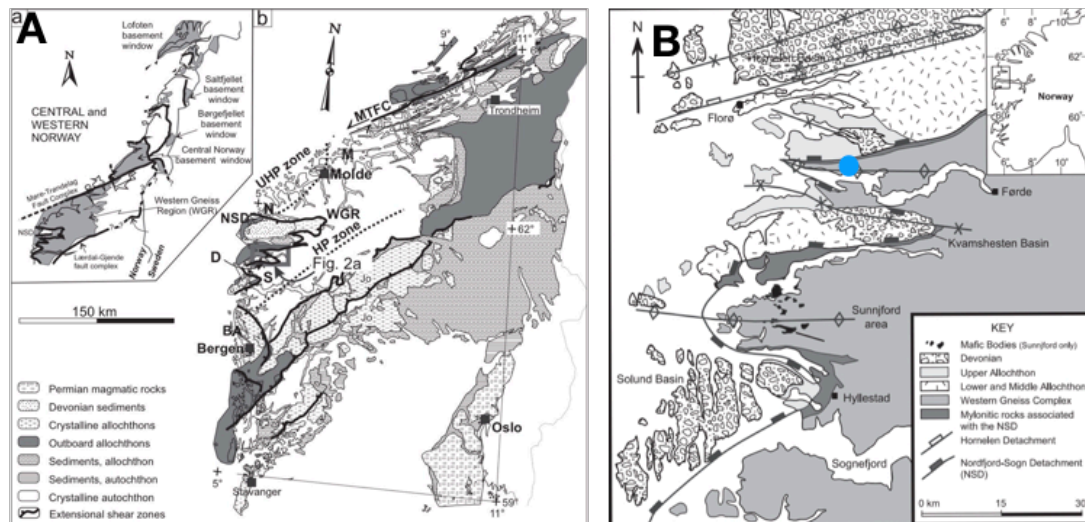


Figure 1. A: Geological map of the western gneiss region. After Braathen et al., 2014. B: Regional geological map of the Nordfjord-Sogn detachment zone. After Foreman et al., 2005. The blue dot in figure B mark the location of Engebøfjellet.

Collision:

The Baltica craton was subducted beneath the Laurentia craton to the west during the Caledonian orogeny (Cuthbert et al., 2000). In the Sunnfjord region where Engebøfjellet is located, pressure recordings show a peak metamorphic pressure of 18kbar. To the north west of this region, recordings show peak pressure above 28kbar (Braathen et al., 2014). This pressure gradient has been interpreted to indicate a north west direction of the subducted slab (fig. 2).

Extension and exhumation:

The period of convergence of Baltica towards Laurentia was followed by a post orogenic regime. Exhumation of the WGR have been explained by several models, one model that seems to be generally agreed upon are the unroofing mechanism along detachment zones.

The Nordfjord-Sogn detachment zone (NSDZ) that are situated close to the Engebøfjellet have been proposed as a possible glide path supporting the unroofing process (Kylander-Clark et al., 2008).

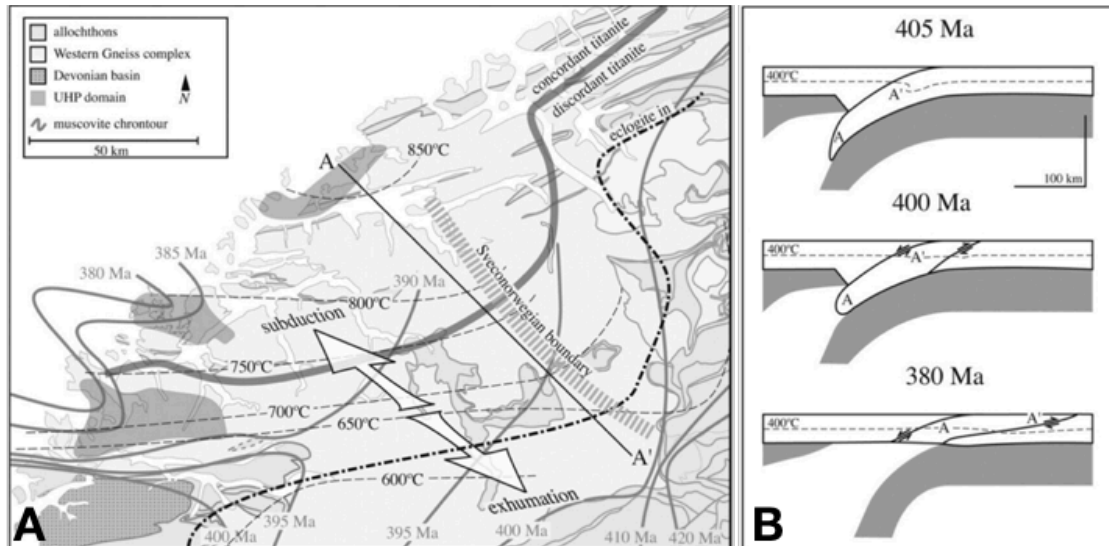


Figure 2. A: The subduction direction of the western gneiss region. The profile A-A' are modelled in cross sectional view in figure B. Subduction temperatures and pressures (and depths) was higher in the north-western part of the WGR. After Kylander-Clark et al., (2008).

2.2 Local geology

Several eclogite bodies occur in the Sunnfjord region, particularly in the Førdefjord (fig.3) and Dalsfjord/Flekke region south of the Førdefjord (fig.1b) (Korneliussen et al., 2000). In addition to the Engebøfjellet eclogite in Naustdal, the Drøsdal eclogite in Flekke have been well studied (Foreman et al., 2005).

The eclogites in the Sunnfjord region, marked as black lensed in fig.3, have been interpreted to originate from mafic intrusions with a gabbroic composition. Dating of zircon at Engebøfjellet and Sm-Nd ages of one eclogite in the Dalsfjord area give ages at ca 1500Ma for these intrusions (Korneliussen et al., 2000).

The bedrock units in the Førdefjord region consists of granitic and granodioritic gneisses, amphibolite and metagabbro (Fig.4) Eclogite lenses including the Engebøfjellet eclogite are hosted within these lithologies.

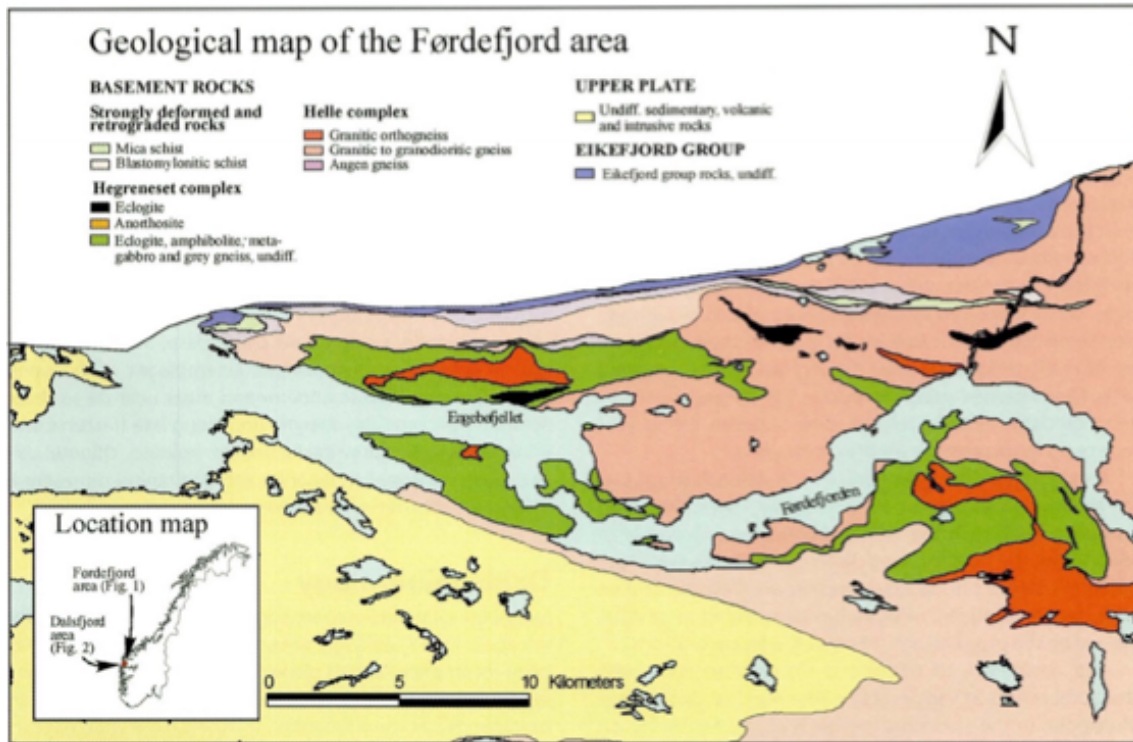


Figure 3. Geological map of the Førdefjord area. After Korneliussen et al., (2000).

2.3 The Engebø Eclogite

Engerbøfjellet is situated on the north side of the Førdefjord in Naustdal, Sogn og Fjordane, Norway. The Eclogite body is lens shaped and follows the geometry of the Engebøfjellet mountain ridge (Korneliussen et al., 2000) (fig.4). Engebøfjellet are exposed beneath the NSDZ (Nordfjord Sogn Detachment Zone) boundary (Braathen et al., 2014) (fig. 1). The approximate NSDZ contact is marked by the presence of phyllonite and blastomylonitic gneisses, upper plate rocks are exposed above the contact (Braathen et al., 2014).

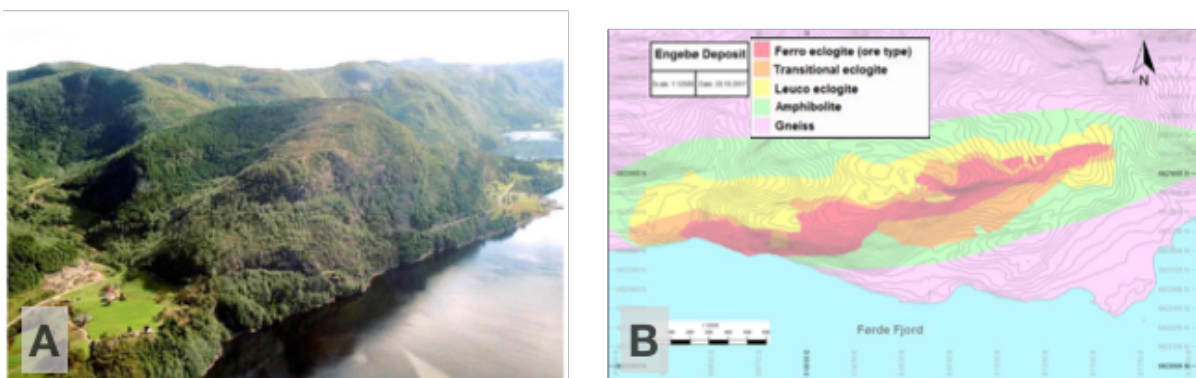


Figure 4. A Aerial view of the Engebøfjellet. B: local geology of the Engebøfjellet ridge. Both after Nordic Mining ASA (2016).

There are two main eclogite types making up the eclogite lens at Engebøfjellet. The most important in an economic perspective is the ferro-eclogite. Ferro-eclogite have more than 3% TiO₂ and make up the central parts of the eclogitic body (red color in fig. 4b). Leuco-eclogite have less than 2% TiO₂ (yellow color in fig.4b). This eclogite type is dominant in the outer parts of the west flank of the lens. The eclogite body is surrounded by amphibolites, dioritic gneiss and granitic augen gneiss, which have smaller lenses of retrograded eclogite (Braathen et al., 2014).

The structural and metamorphic history of Engebøfjellet have been illustrated by Braathen et al., (2014). They found six stages of deformation occurring during the exhumation from peak metamorphic conditions. Thermobarometry was applied to mineral textures corresponding to these six deformational stages. An overview of the temperature and pressure estimates are shown in table 1, and the steps are visualized in figure 5.

Table 1 Deformation events that occurred at Engebøfjellet during exhumation after Braathen et al., (2014).

Metamorphic stage		Pressure (Mpa)	Temp C
Eclogite facies	D1+D2	1550-1800	600
Garnet amphibolite facies	D3	800	525-540
Epidote amphibolite facies	D4	700-800	500-525
Greenschist facies fracturing.	D5	300-400	300

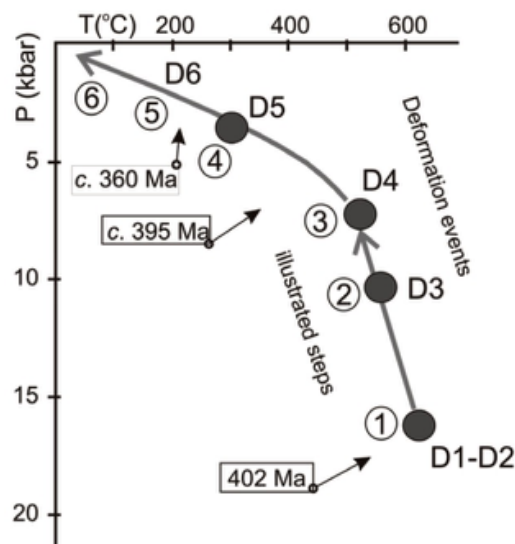


Figure 5. The illustrated exhumation path of Engebøfjellet. Steps D1-D6 is referred to in table.1. After Braathen et al., 2014.

2.4 The ore forming processes at the Engebøfjellet Eclogite

No pre eclogitic gabbroic mineral assemblages have been observed or described from Engebøfjellet in the previous studies mentioned in this thesis (Korneliussen et al., 2010);(Kleppe 2013); (Braathen et al., 2014). Extensive deformation and metamorphism have likely caused complete overprinting of such features. This complicates the interpretation of the ore forming processes.

Incomplete eclogitization of gabbro are seen in the Flekke area 30-40 km south of Engebøfjellet (Korneliussen et al., 2000). Ferrogabbroic rocks and partly eclogitized gabbros show enrichment in magnetite-ilmenite mineralization that occurs as decimeter thick bands. Such bands are discussed in the above-mentioned study to have been formed because of fractionation processes in the gabbroic magma chamber.

The high amount of titanium and iron in the Engebøfjellet eclogite are believed to be related to transformation of a host rock similar to the gabbro observed in the Flekke area. This have led to the hypothesis that the titanium enrichment in the Engebøfjellet eclogite and other eclogites in the area could be traced back to magmatic fractionation within a gabbroic intrusion (Korneliussen et al., 2000).

3 Methods

3.1 Field work

Field work at the Engebøfjellet was done during two days in the early part of the summer 2017 (11th and 12th of June, 2017). Sampling were partly done using a Makita battery powered hammer-drill. This drill was fitted with a wide (4-5cm) hollow drill bit, making it possible to extract shallow (3-4 cm deep) drill core sample from surfaces. The aim for the field work was to find samples where rutile had been precipitated in veins. Furthermore, eclogite rock without vein textures, what was interpreted as “fresh eclogite” was collected. In addition to the surface samples, Nordic Mining provided access to the drill core archives in their office in Naustdal for selection of necessary additional samples.

3.2 Optical microscopy

The thin sections were produced at the Department of Geosciences of UiT the Arctic University of Norway, Tromsø. 23 samples were cut into suitable slabs and delivered to the lab for thin section preparation.

Optical microscopy was used to observe mineral relationships of the studied samples. It was also used to select areas of interest for further studies with LA-ICP-MS or SEM. The optical microscope was also used to search for suitable samples to prepare for fluid inclusion studies.

Petrographic microscopes from the brands Zeiss and Leica was used, both reflective and transmitted light was used. The reflected light was used because of the relatively common isotropic minerals (ilmenite vs pyrite). The reflected light microscope can be used to separate individual isotropic phases with anhedral crystal shapes. The lenses 4x, 10x and 20x was used.

3.3 SEM / EDS

The scanning electron microscopes with the electron back scatter electron detector (BSE) give grayscale images with high resolution. The Energy-Dispersive X-Ray Spectroscopy detector (EDS) provide elemental analysis of selected spots or a group of spots to make an element map. Additionally, single spot analysis of major elements using the EDS detector was done to obtain composition of symplectite.

Analytical conditions for EDS

The microscope used was “SEM Zeiss Merlin VP compact” located at the UiT - department of geosciences. The acceleration voltage was 20 kV, aperture was 60 microns, working distance 8.5mm. Samples was coated with a layer of 20nm carbon. Results was exported to the software AZtec by Oxford instruments.

3.4 Fluid inclusions

The main objective with this method was to analyze minerals found in quartz veins for traces of fluids that circulated in the eclogite veins and became entrapped during vein mineral growth. The vein minerals, mainly quartz and carbonate were selected from veins seen in outcrop scale and also from vein textures seen in the drill core samples.

The goal for using this method was to produce data that could place constraints on the physical conditions for fluid circulation. Together with thermobarometric data fluid inclusion studies can give insights into the temperatures and pressures of formation. Furthermore, it can give the salinities of the fluids that circulated in the system at the time the observed mineral crystallized. Such constrains can be valuable to the understanding metasomatism in eclogites.

The measurements of fluid inclusions were done at UiT, department of Geology. The measurement of fluid inclusions was performed by a research assistant under the supervision of associate professor Sabina Strmic Palinkas. The prepared sections were placed in a cooling and heating Linkam TH 600 stage. This instrument allows cooling to temperatures of -180°C by introducing liquid nitrogen to the chamber. The chamber also has a small heating stage that allows controlled heating up to 600°C. The fluid inclusion stage is equipped with an Olympus BX-2 microscope. Computer software was used to control the cooling and heating rate.

Sample preparation.

Suitable samples were grinded and polished with gradually finer abrasives on a rotary polishing table. When sufficient polishing was achieved, the adhesive crystal bond was used to fix the rock cube to a glass plate.

The thickness reduction was done using a diamond edged saw. This stage reduces the thickness of the sample to approximately 1mm. The sample needs to be thin enough to enable the observer to clearly see through it with a optical microscope. A coarse rotary grinder were used to further reduce the sample thickness considerably before polishing.

After both sides was polished, the sample was removed from the glass plate by heating it to 90°C, which caused the adhesive to melt. Care was taken to avoid excessive heating to make sure the fluid inclusions avoided unwanted cracking from boiling and internal pressure build ups. Left over traces of glue on the surface of the samples was removed using acetone.

3.5 Major and trace element analysis

Major and trace element analyses was performed by Activation Laboratories, a commercial lab located in Ontario, Canada. Trace and major element analysis were applied to seven eclogite samples (four ferro-eclogite and three leuco-eclogite samples). Two rutile crystals and three carbonate samples were also analyzed for their trace element composition. The objective was to use this data to compare trace element behavior between the high and low grade rock.

Actlabs have pre-defined analytical packages (*Activation laboratories, 2018*). The analytical packages “*4B2-research*” was applied to the monomineralic samples, and “*4Lithoresearch*” was applied to the whole rock samples.

Both methods use analytical equipment produced by the manufacturer Perkin Elmer, the model used are either Sciex Elan 6000, 6100 or 9000 ICP/MS. (*Activation Laboratories, 2018*). The prepared sample materials was mixed with lithium metaborate/tetraborate in graphite crucibles and heated to 1150 degrees in an induction furnace, this procedure promotes fusing. Fused material is added to a 5% nitric acid and dissolved, the dissolved solution are analyzed for its elemental composition using either the ICP-OES or the ICP-MS method.

ICP (Inductively Coupled Plasma)

Plasma is a gas that becomes electrically conductive under an electromagnetic field. Argon gas is commonly used as a plasma forming gas in the ICP-MS and ICP-OES methods. Argon is applied to a conductive coil, and are ignited by an electric current. Which then burns at a very high temperature.

ICP-OES (Optical mass spectrometry)

The sample solution is heated and are introduced to the plasma in a vapor state. The collision between the high energy inductive plasma and the molecules in the vapor causes the molecules in the solution to break down into atoms, and the electrons to be separated from their atoms before suddenly being rearranged. The energy produced by this electron jump is emitted as light. Each atom has a specific light spectrum, and these spectras can therefore be recorded by sensors and used to fingerprint the elemental composition of a sample in solution. ICP-OES have a lower detection limit than ICP-MS. For the purpose of major element composition analyses ICP-OES is suitable, but trace element analysis should use the ICP-MS method.

ICP-MS (Mass spectrometry)

Instead of using a light spectrum to analyze elemental composition, this method extract ions after they have been separated from their molecules in the plasma and guides them into a mass spectrometer. In a mass spectrometer, ions are separated based on their mass to charge ratio and their abundance are recorded by sensors.

Sample preparation

A low amount of sample material was needed for litho geochemistry (10 g/sample). The samples were therefore cut with a rock saw and crushed using a hammer on a steel plate instead of the jaw crusher to avoid sample loss. The crushed material was milled with an agate mill to a fine powder and prepared for shipment to the lab in sample bags. The steel plate, hammer, a brush, and a agate mill was carefully cleaned between samples.

A note about an attempted method:

An attempted sorting of individual minerals (garnet, omphacite and rutile) from the eclogite matrix of leuco and ferro-eclogite was conducted in the early part of lab work for this thesis. The aim for this method was to analyze the trace element composition of each mineral fraction in the ferro and leuco-eclogite. This method was discarded because of the observed impurities in the sorted minerals. To avoid impurities, the fractions needed to be crushed to sizes that was too small for efficient manual sorting of the samples. Larger impurity free mineral phases were found to occur too rarely in the crushed material to defend the further use of time for this method. Actlabs needed 0.5g of sample material to perform trace element analysis of monomineralic samples. This might have proved a viable method if the required sample material was significantly less.

3.6 La-Icp-MS

The abbreviation LA-ICP-MS stands for “laser ablation inductively coupled mass spectroscopy”. The ICP and MS part of the abbreviation have previously been explained. Laser ablation means that instead of dissolving the analyzed material in a solution, a high energy laser heats and dissolves the sample where it is pointed. The elements are collected by a carrier gas encapsulated by a chamber and are from there introduced to a plasma and analyzed in a similar process as previously explained in the litho geochemistry section.

Rutile, ilmenite, garnet and omphacite from the matrix of both types of eclogite at the Engebøfjellet was ablated. The purpose of using this method was to enable more detailed trace element analysis than whole rock litho geochemistry would allow. Furthermore, this method would enable the interpretation of trace element behavior of texturally different rutile.

Analytical conditions for LA-ICP-MS measurements

A guide that explained which points in the thin sections that should be ablated was produced and sent to the LA-ICP-MS lab at the Geological Survey of Finland for analysis. The explanation of the analytical condition and analytical procedure was provided by the lab, and are reproduced here:

Laser ablation single collector ICP-MS analyses of the selected minerals were performed at the Geological Survey of Finland (GTK), using a Nu AttoM SC-ICPMS (Nu Instruments Ltd., Wrexham, UK) and an Analyte 193 ArF laser-ablation system (Photon Machines, San

Diego, USA). The laser was run at a pulse frequency of 10 Hz and a pulse energy of 5 mJ at 40% attenuation to produce a energy flux of 3.5 J/cm² on the sample surface with a 50 and 25 µm spot size. The laser was automatically switched on for 40 seconds for signal acquisition and then off for 20 seconds for background levels to be attained and measured. Analyses were made using time resolved analysis (TRA) with continuous acquisition of data for each set of points (2standards, 15 unknown , 1 quality control standard). The solid synthetic silicate NIST612 and BRC2-G standard has been used for external standardization, while the synthetic glass BHVO-G has been used for quality control. The ²⁹Si and ⁴⁹Ti have been used, as an internal. The measurements were performed over 55 isotopes and 38 elements at low resolution ($\Delta M/M = 300$) using the fast scanning mode. Data reduction was handled using the software GLITTER™ (Van Achterbergh et al., 2001) which allows the baseline subtraction, the integration of the signal over a selected time resolve area and the quantification using known concentrations of the external and internal standards.

3.7 Stable isotopes analysis

Sample preparation

Vein carbonate from drill core samples kgr11, kgr13 and kgr15 was selected, a small amount of powder (2-3g) was extracted from two spots at each drill core sample. The two spots from the same drill core was located close to each other (2-5 cm apart). Duplicates was produced for each individual powder material. One random sample was replicated by the lab as an additional quality control test making a total of 13 analyzed carbonate samples for the $\delta^{13}\text{C}$ and $\delta^{18}\text{O}$ isotopic composition.

The carbonate was extracted by cutting suitable pieces with a saw. These pieces was crushed to a powder using an agate mill. The sliced drill core pieces were washed with tap water and dried prior to crushing. The agate mill was cleaned using a clean cloth and ethanol in between samples. The duplicates were produced by halving the crushed material for each of the six samples.

Analytical method

The stable isotope analysis was performed at The Stable Isotope Laboratory at CAGE – Centre for Arctic Gas Hydrate, Environment and Climate located at UiT – The Arctic University of Norway, in Tromsø, Norway.

The analytical procedure are described by the lab and reproduced here: No pre treatment was performed. Carbonate samples are placed in 4.5mL vials. The vials are flushed with He, and 5 drops of water free H₃PO₄ are added manually with a syringe. After equilibration >2h at T = 50C, the samples are analysed on Gasbench II and MAT253 IRMS. Normalisation to VPDB by 3 inhouse standards with $\delta^{13}\text{C}$, $\delta^{18}\text{O}$ values that enclose the samples. The inhouse standards have been normalized by several international standards. Instrument uncertainty (ThermoScientific) $\delta^{13}\text{C}$, $\delta^{18}\text{O}$ is standard deviation ≤ 0.1 ‰. Uncertainty in $\delta^{13}\text{C}$, $\delta^{18}\text{O}$ for heterogeneous samples/small samples may be larger. The instrument used for the analysis was Thermo Scientific MAT253 IRMS + Gasbench II.

4 Theoretical background

4.1 The formation of eclogites

Eclogites are plagioclase free metamorphic rocks with a garnet and omphacite content that are above 75wt % (e.g., Miller et al., 2007). Eclogites have a mid ocean ridge basalt (MORB) - like bulk rock chemistry and can also be characterized with their higher density than the asthenosphere (Hacker et al 1996).

The eclogitization process is a densification process. As the densification of the protolith to eclogites occur, a volume reduction takes place to accommodate for the higher density of eclogite minerals. This volume reduction and mineral transformation reaction are accompanied by the release of volatiles (Philippot et al., 1990).

These characteristics have given eclogites a key role in understanding geodynamics. Because of their negative buoyancy compared to the asthenosphere, the densification mechanism are believed to be one of the driving mechanisms behind the slab pull part of plate tectonic movement. The release of fluids at depths in subduction zones have been used as an explanation for the genesis of subduction zone magmatism (John et al., 2003).

The volume reduction during eclogitization occur even though these reactions involve hydration reactions (Jamtveit et al., 1990). Some eclogitic protolith such as basalts are rich in volatiles from seafloor alteration, others (such as gabbroic intrusions) are dry prior to metamorphism (John et al., 2003).

The transformation of a dry gabbro to eclogite was studied by John et al., 2003. These authors found that the fluid rock ratio acting on the gabbro was essential in initiating eclogitization reactions. They found textural evidence that gabbroic rock which had been subjected to eclogite forming pressure and temperatures had either overstepped the eclogitization reactions or had incomplete reactions. Thus, implying the essential role of the introduction of external fluids to the gabbro system for eclogite transformation reactions to take place.

The physicochemical processes that leads to eclogite transformation was also discussed by Bjørnerud et al., (2002). These authors discussed the importance of a fluid front in the efficiency of the eclogitization mineral reactions. The surface area of the fluid front acting on

the unaltered protolittic assemblage are important for the rate of eclogitization.

Transformation to eclogite with the introduction of fluids through shear zones are an order of magnitude faster than the introduction of fluids through simple fracturing, because of the larger contact area of fluid/rock in shear zones (Bjørnerud et al., 2002). Fluids can fracture rock if the internal pressure of the fluid exceeds the compressive stresses of the rock while the internal stress of fluid exceeds tensile strength of the rock (Philippot et al., 1991).

In addition to fluid induced eclogitization, the mineral reaction can also be driven by diffusion processes. Diffusion reactions work on much slower time-frames compared to fluid induced reactions (Bjørnerud et al., 2002). The significance of this type of transformation process is therefore governed by the residence time of the eclogite at eclogite facies temperature and pressure conditions. This is supported by the textural evidence suggesting that gabbro can survive eclogite facies conditions without transforming to eclogite (John et al., 2003).

4.2 Mobility and behaviour of trace elements in hydrothermal conditions.

For this study the definition of mobility is used after Van Baalen (1993) “An element is considered mobile if measurable changes in concentrations relative to a specified reference frame occur during a particular process”.

Solubility in hydrothermal systems

The solubility is defined as the upper limit (amount) of a fluid's ability to hold the element. (Wood et al., 1998);(Robb., 2004). Temperature, pressure, pH and redox potential are important factors for element mobility and the dissolution and solubility of minerals in fluid (Seward et al., 2014). In addition to these factors, the presence of ligands and other complexing agents can increase solubility of some elements in solutions (Van Baalen 1993), including titanium (Ryzhenko et al., 2004).

H₂O as an agent for mineral dissolution and transport.

Water has the ability to act as a solvent in the dissolution and transport of elements. The ability of water to act as a solvent is mainly attributed to its ability to stabilize and bond to atoms and molecules that have a charge (Seward et al., 2014).

Water molecules can form networks of hydrogen bonded H₂O molecules (Seward et al., 2014). This is caused by the characteristic dipole moment of H₂O molecules. H₂O molecules

are not symmetrical, this is the reason for the special characteristic of the H₂O molecule where the center of the negative and positive electrical field does not coincide (Robb., 2004). In the presence of an electrical field, or charged ions, the water molecules can align themselves around ions increasing their stability in water (Robb., 2004).

Water have the ability to self-ionize. Self-ionization involves the loss of a proton from the water molecule, causing the formation of a charged hydroxide ion (OH⁻) (Seward et al., 2014). The stability of species such as AlOH²⁺ or FeOH³⁺ depends on the concentration of OH⁻ ions in solution. The ability of water to self-ionize is a function of the availability of NaCl, and the pressure and temperature acting on the solution (Seward et al., 2014).

Ligands and complexing agents.

Ligands are atoms or molecules that have the ability to act as an electron donor for a metal, forming covalent bonds, or metal complexes (Masterton et al., 2012). The most important ligands are Cl⁻, HS⁻ and OH⁻. Many more exist as variations of sulfur species, thioanions, fluoride, carboxylates (Seward et al., 2014). The ligands can bond to ions of opposite charge and act as transport capsules for these elements in solution.

Mobility of REE in hydrothermal systems

The main transport mechanisms for REE (rare earth elements) are complexation by chloride and sulfate. In the sulfate complexes the solubility of all REE are broadly the same. Chloride complexes show preferential solubility with the light REE (LREE) compared to the heavy REE (HREE). This property of the REE could lead to fractionation of these elements in the presence saline fluids (Migdisov et al., 2016).

Mobility of trace elements metasomatic fluids found in eclogite.

The mobility of high field strength elements in a contact aureole surrounding a quartz vein in eclogite was studied by Gao et al., 2007. These authors found a depletion in trace element composition in all trace elements except Hf and Zr in the eclogite host rock surrounding the quartz vein (fig.6). This depletion was interpreted to have been caused by leaching of the rock by fluid.

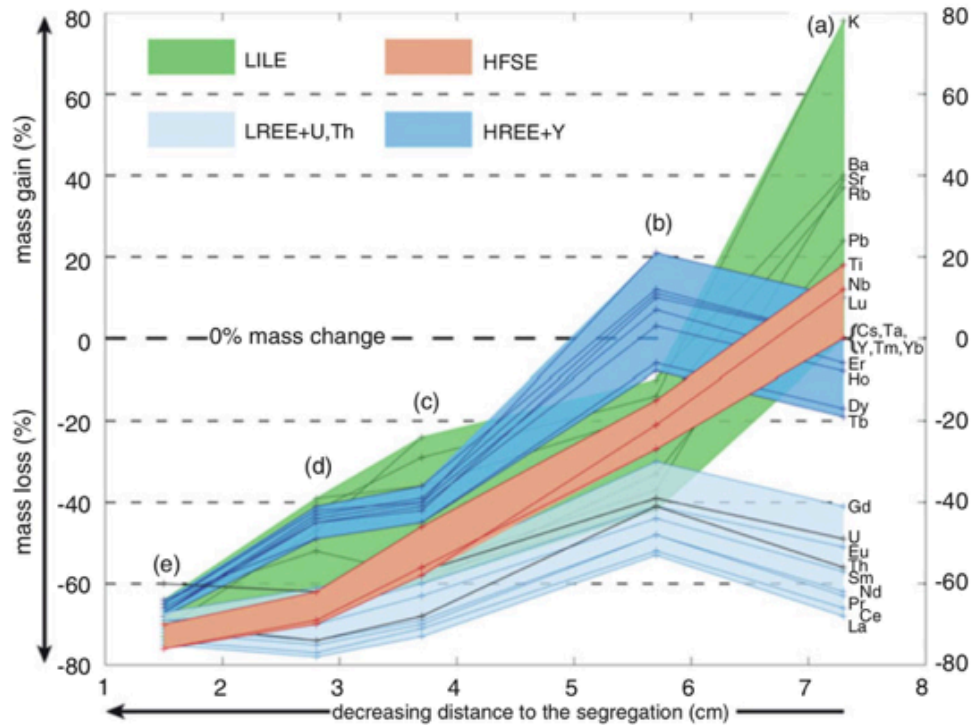


Figure 6: The mobilization of trace elements relative to Zr and Hf (0 mass change line) in eclogite host rock in cm distance away from a rutile bearing vein segregation. After Gao et al., (2007).

4.3 Fluid inclusions

Fluids that circulate in rocks can become encapsulated by minerals during mineral growth. These inclusions can act as barometers to study the temperatures and pressures under which they were entrapped. There are three main groups of fluid inclusions; primary fluid inclusions, secondary fluid inclusions and pseudosecondary fluid inclusions (Shepherd et al., 1985).

Primary fluid inclusions are formed during the crystallization of the host mineral, and are a direct consequence of entrapment of the fluid from which the mineral crystallized. These inclusions often grow parallel to the crystal faces and can be seen as chain like tabular lines (Bodnar 2003a). They can also be seen as individual, large inclusions with no grouping or growth pattern, in the center of minerals (Bodnar 2003a).

Secondary fluid inclusions are related to fluids that have infiltrated the crystal after the host mineral had crystallized. This can occur through fluid infiltration along fractures and cracks in the mineral that was later sealed. These inclusions can have similar morphology as the bands seen with primary inclusions. Primary inclusions will however not cross cut the crystal face,

as the secondary inclusions will.

Pseudosecondary fluid inclusions are inclusions that were entrapped during fracturing that happened at the same time as mineral crystallization. The pseudosecondary inclusions are thus a hybrid between primary and secondary fluid inclusions. A schematic overview of these inclusion types can be seen in fig.7.

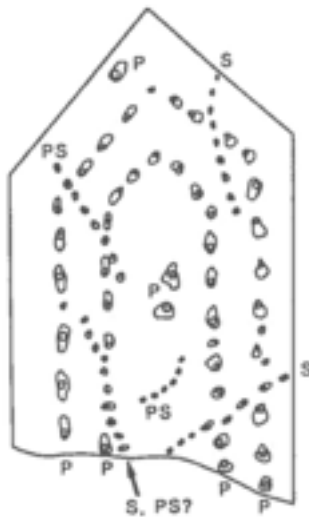


Figure 7. (After Shepherd et al., 1985)

Primary fluid inclusions are used as markers for the chemical composition of the fluids that circulated during the growth of the host mineral. Secondary fluid inclusions can be used to approximate the compositions of fluids that circulated during a metamorphic event that caused fracturing.

Fig.7 shows the relationship between the classes of fluid inclusions and the growth zoning of the crystal and cracks propagating inward from the crystal phase. S = Secondary, PS = pseudosecondary and P = primary.

Phase relation classification of fluid inclusions

The phases liquid, vapor or solid can be entrapped within the inclusion. At room temperature, the relationship between these phases is the basis for a classification of inclusions on phase relationships. Phase relationships can be important for the origin and interpretation of fluid events, and it is an early *means* to group inclusions that we believe have been trapped under similar conditions in terms of temperature, pressure and chemical composition.

Inclusions can be classified in the following three categories:

1- *Monophase inclusions* (L, S, V) completely filled with either liquid, vapor or solid.

2- *Two phase inclusions* (L + V) consisting of mainly liquid and a vapor bubble, this is the most common type of phase relation seen in fluid inclusions. Rarely this can be seen as a mineral entrapped within a liquid.

3- *Polyphase inclusions* ($S + V + L$, $S + L_1 + L_2$) Consisting of three or more phases. The solid phase can be a daughter crystal that have crystallized from the fluid that was entrapped, or small impurities that was trapped by the mineral during fluid inclusion formation.

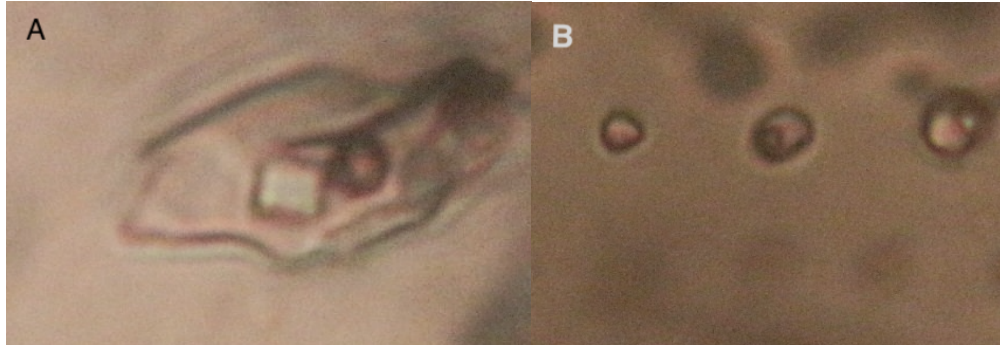


Figure 8: The width of both photographs is $30\mu\text{m}$. A: Polyphase inclusion from Engebø quartz veins (this thesis). The square is a halide crystal of unknown composition, the sphere is vapor and these two phases sits in the fluid inclusion which is bordered by a dark boundary to the rest of the crystal. B: Show three, two phase inclusions with small vapor bubble within a liquid inclusion.

4.4 Fluid inclusion microthermometric measurement and analysis.

Microthermometric measurements involves the careful observation of phase changes in the inclusions and recording of the temperatures. We use these data points as input together with equations of state to output the characteristics of the inclusions such as salinity and the isochore of the fluid (Brown et al., 1989). The type of data points that are needed to analyze the formation conditions of inclusions depends on the specific chemical composition of the fluid inclusions. Inclusions belonging to different chemical systems require different analytical procedures.

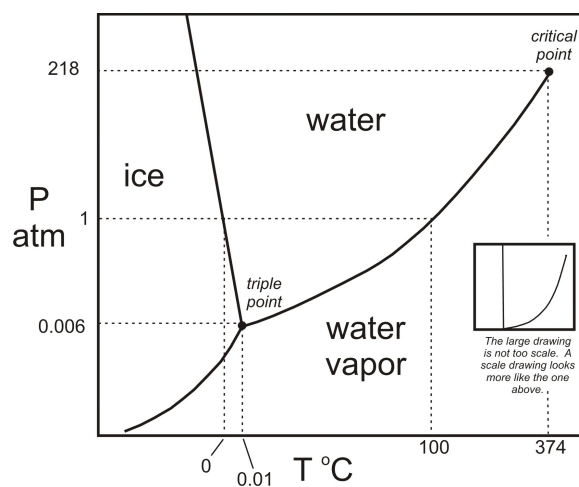


Figure 9. Phase diagram of water. After serc.carleton.edu, 2018

Fig.9 show a phase diagram of water in the P-T space. Lines represents boundary conditions between the stable phases. Equations of state enable us to relate experimental results of phase relationships to models and thus make extrapolations of our results to areas in the P-T field where experimental results may not exist. The same principles govern the systems with more variables such as NaCl and CO₂ components.

4.4.1 Recording data

A temperature chamber allows for controlled freezing and heating of the fluid inclusion sample. This section presents the parameters that are recorded during the freezing run and later the heating run.

Phase transitions should not be recorded during the initial freezing of the inclusions, this is to avoid the effect of metastability (e.g., Fall et al., 2011). Metastability can increase the stability of water outside its true stability field, such that it freezes at lower temperatures than it should. To avoid this effect the inclusion is rapidly frozen to temperatures at around -100 °C and kept there for a couple of minutes. Phase changes are recorded during re-heating of the frozen inclusion.

The sudden appearance of a liquid phase within the ice structure of the inclusion marks the first melting temperature. This temperature corresponds to the eutectic temperature of the inclusion system and are marked as (T_E). The eutectic temperature for a range of different salt solutions have been found experimentally. The eutectic temperature can therefore be used as an approximation for the general chemistry of the inclusion system (table.3) (Shepherd et al., 1985).

Table 2. The relationship between eutectic temperature of salt inclusions and the type of salt of the system. Modified after (Shepherd et al., 1985);(Borisenko., 1977).

Salt system	Eutectic Temperature °C (T _e)
H ₂ O-NaCl-CaCl ₂	-55
H ₂ O-MgCl ₂ -CaCl ₂	-52,2
H ₂ O-KCl-CaCl ₂	-50,5
H ₂ O-CaCl ₂	-49,5
H ₂ O-Na ₂ CO ₃ -K ₂ CO ₃	-37
H ₂ O-NaCl-FeCl ₂	-37
H ₂ O-FeCl ₂	-35
H ₂ O-NaCl-MgCl ₂	-35
H ₂ O-MgCl ₂	-33,6
H ₂ O-NaCl-KCl	-23,5
H ₂ O-NaCl-Na ₂ SO ₄	-21,9
H ₂ O-NaCl-NaHCO ₃	-21,7
H ₂ O-NaClNa ₂ CO ₃	-21,8
H ₂ O-NaCl	-21,2
H ₂ O-KCl	-10,6
H ₂ O-NaHCO ₃ -Na ₂ CO ₃	-3,3
H ₂ O-NaHCO ₃	-2,3
H ₂ O-Na ₂ CO ₃	-2,1
H ₂ O-Na ₂ SO ₄	-1,2

The ice melting temperature (**T_{MICE}**) is the temperature where there is no traces of ice in the inclusion. In addition to regular H₂O-ice, we may also see hydrohalite and clathrate. In cases where we have several of these ice phases we need to make note of each individual ice melting temperature. Hydrohalite melting (**T_{MHH}**) are technically difficult to observe, because it needs indirect observation of changes in the surrounding phases. Relatively few observations of hydrohalite have been reported in the literature (Bodnar., 2003b).

If the inclusion contains CO₂, we can expect to see signs of clathrate. Clathrate are a hydrate ice structure that incorporates CO₂ and H₂O molecules into its crystal lattice, but rejects salt ions (Fall et al., 2011). The melting parameter are noted as **T_{MCLAT}**. The technique for recognizing clathrate are presented in (Fall et al., 2011).

Upon heating of the sample, we want to record the timing of homogenization of inclusion phases. Homogenization can be defined as the point where phases stop to coexist and are moved into the stability field of either vapor or liquid in expense of the other phase. We differentiate between the early homogenization temperature of individual phases (such as CO₂ in a CO₂-NaCl-H₂O system), and the total homogenization temperature of the inclusion (**T_HTOT**). The homogenization into a vapor phase occur only if the inclusion is already vapor dominated i.e ($V > 60\%$) (Shepherd et al., 1985). For a system consisting of CO₂ we need to record the early homogenization temperature of the CO₂ phase (**T_HCO₂**). The salt dissolution temperature (**T_HNaCl**) marks the temperature of the disappearance of a halite crystal. The salt dissolution temperature can be used for the determination of inclusion salinity (Bodnar., 2003b).

4.4.2 The NaCl-H₂O System.

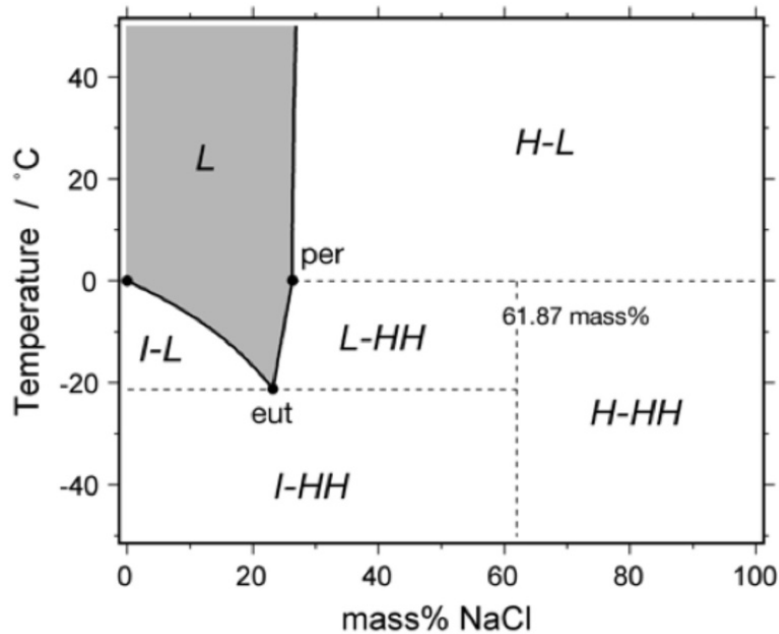


Figure 10: T-X diagram of the NaCl-H₂O system. L = liquid, H= halite, HH= hydrohalite. I=ice. Eut = eutectic point, Per = peritectic point After Bakker., (2012).

Figure 9 show the relationship between temperature of phase transitions, and the salinity of the NaCl-H₂O system. First sign of fluid will appear in the eutectic temperature. Whether hydrohalite or ice will be present after the eutectic temperature have been reached, are dependent on the salinity of the system.

Methods to determine salinity exists for the three fields shown in contact with liquid in fig.10 (A: 0-23.2 wt.% , B: 23.2-26.3 wt.5 and above C: 26.3wt%.) To decide which system the inclusion belong to we need to observe the timing of the disappearance of the phases; Ice, hydrohalite and halite (Bodnar., 1994). If ice is the last phase to disappear, the system belongs to category **A**. If hydrohalite is the last phase to disappear, the system belongs to category **B**. If there are halite daughter crystals in the system, and this is the last phase to disappear upon heating from a frozen state, the inclusions belong to the category **C**.

4.4.3 The CO₂-NaCl-H₂O system.

In the CO₂ system, the effect of clathrate formation must be considered in salinity estimates. Consumption of H₂O in the clathrate structure will increase the salinity of the residual liquid. Ice that crystallize from this liquid will therefore not represent the true salinity of the system (Diamond., 1992).

To enable precise correlation of salinity with clathrate melting temperature, the clathrates needs to melt in the presence of liquid CO₂ only or gaseous CO₂ only (Fall et al., 2011). The NaCl will not enter the clathrate structure (Diamond., 1992), we can therefore treat the CO₂-H₂O-system as a sub system within the total H₂O-NaCl-CO₂ system. The stability of Clathrate in this subsystem depends on the H₂O activity variable. H₂O activity in the fluid inclusion are reduced with the addition of NaCl, thus the clathrate melting temperature are reduced with the presence of NaCl (fig.10) (Diamond., 1992).

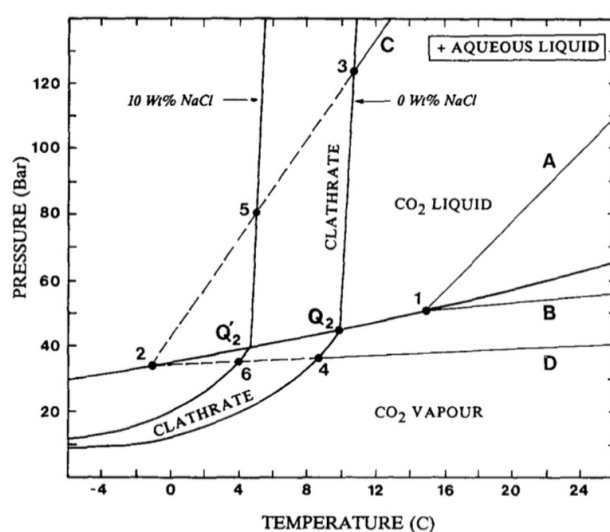


Figure 11: Phase diagram showing the stability fields of clathrate in a solution with 0 wt% NaCl, (Q₂) and 10 wt% (Q'₂). After Diamond., (1992).

4.4.4 Calculating salinity, density and the isochore.

The determination of salinity and density for H₂O-NaCl inclusions, (and some CO₂-H₂O-NaCl inclusions) was done using the “HOKIEFLINCS_H2O-NACL” a Microsoft Excel spreadsheet for interpreting microthermometric data from fluid inclusions based on the PVTX properties in the H₂O-NaCl system (Steele-MacInnis et al., 2012). Equations of state are built in to the spreadsheet.

Some inclusions containing CO₂, missed recordings of the CO₂ homogenization temperature, a parameter needed to determine the salinity from the clathrate melting temperature with the use of equations of state. Bozzo et al., (1975), described a method to fit the melting temperature of clathrate to experimental results, extrapolating clathrate melting temperature to salinity using their statistical relationship (eq.1). This equation does not take into consideration the aspect of variable CO₂ and H₂O incorporation into clathrate (Diamond.,

1992). In the Bozzo et al., (1975) study, the relationship was defined for fluid inclusions with salinity up to 16 wt.%. The maximum margin of error reported was 5.7 wt.%, average standard deviation was 2.1%. Although this method have flaws in its accuracy because it does not consider variations in CO₂/H₂O ratio, it was used for this study to obtain an approximation of salinity for inclusions that lacked ThCO₂ measurements. In future sections, this group of inclusions will be referred to as “Category D” inclusions.

$$\text{Eq. 1} \quad \text{Wt \% NaCl} = 0.05286 (10-t)(t + 29.261) \quad \text{After Bozzo et al., (1975)}$$

Where T= Clathrate melting temperature.

CLATHRATES, a package of computer programs for fluid inclusion analysis was used to find the density and salinity of H₂O-CO₂-NaCl inclusions (Bakker., 1997). With the input of the clathrate melting temperature, the CO₂ homogenization temperature, the final homogenization ThTOT, and the approximate volumetric relationships between CO₂ and H₂O after clathrate melting. The salinity and density of the aqueous solutions was found using a set of equations of state. The equation of states after Duan et al., (1992a, b) and Duscheck et al., (1990) was used.

After the above-mentioned steps was performed, the isochores was found using the Fluids1 package with the ISOC program after Bakker (2003). The slope of the isochore was determined by calculating six points in the P-T space for each individual inclusion. These points were calculated with the ISOC program using the built in equation of state after Zhang et al., (1987). The type of host mineral for the inclusions was not considered in the calculated isochore data.

5 Results

5.1 Field observations and sample overview.

Table 3: Overview of samples collected in the field.

Sample ID	UTM coordinates	Sample description
KGR1	32V 0310161-6822750	Omphasite vein, with large elongated crystals
KGR2A	32V 0310131-6822764	Large quartz vein, sample taken from the boundary of vein towards eclogite.
KGR2B	32V 0310131-6822764	Rutile collected from a quartz vein
KGR2C	32V 0310131-6822764	Quartz
KGR3	32V 0310210-6822795	Omphasite vein with amphibole and rutile.
KGR4A	32V 0310173-6822850	Rutile bearing quartz material. Sample is taken from contact with what have the appearance of high grade ferro eclogite. (The vein material was in contact with eclogite):
KGR4B	32V 0310173-6822850	Quartz and omphacite
KGR4C	32V 0310173-6822850	A 2kg block of eclogite, with domains of rutile bearing omphasite rich segregations.
KGR4D	32V 0310173-6822850	Eclogite block picked from blast area. Contains domains of rutile bearing qtz, and Omp in contact with eclogite.
KGR4E	32V 0310173-6822850	Block of brown-yellow mica.
KGR5A	32V 0310185-6822834	Part of shear zone, eclogite with garnet and omphacite segregated domains.
KGR5B	32V 0310185-6822834	Deformed quartz vein within shear zone system.
KGR5C	32V 0310185-6822834	Brown mineralogy, easily drilled, interpreted to be highly weathered.

Table 4: Overview of samples collected from Nordic Mining drill core storage.

Sample id	Drillcore number	Sample depth (meters)	Description
KGR11	Eng16.004	253.40	Carbonate, quartz, omphasite
KGR12	Eng16.022	94.07	Carbonate, quartz with rutile.
KGR13	Eng16.015	246.85	Carbonate,
KGR14	Eng16.022	9.7	Ferro eclogite
KGR15	Eng16.033	103.10	Carbonate and leuco eclogite
KGR16	Eng16.004	232.95	Ferro eclogite (fine grained, dark color).
KGR17	Eng16.022	018.10	Ferro eclogite (fine grained, dark color).
KGR18	Eng16.033	23.50	Leuco eclogite
KGR19	Eng16.033	60.60	Leuco eclogite



Figure 12: A: Banding of garnet rich zones (red) in eclogite (green). B: Garnet in quartz rich vein. C: Sample krg5. Folded garnet and omphacite rich layers. D: Sample kgr3. Large rutile precipitated in omphacite. E: Sample kgr1. A large omphacite vein. F: Sample kgr2. A large quartz vein with rutile phenocrysts.

A large variation of vein textures was observed in the field in outcrops at Engebøfjellet. Not all was sampled and analyzed. An overview of sample locations and a rough description of each sample are given in table 4 and 5. Figs.12d and 12f show large rutile phenocrysts up to several cm in diameter precipitated in a large quartz vein (12f) and in an omphacite vein (12d). Rutile phenocrysts most often appear along the boundary of the vein-eclogite contacts.

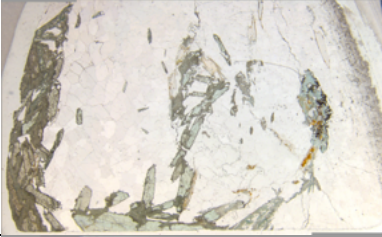
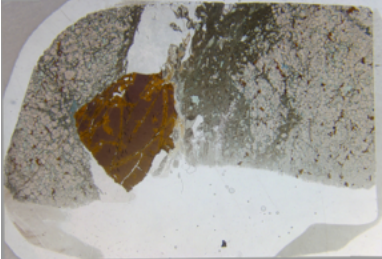
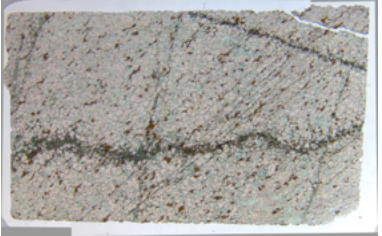
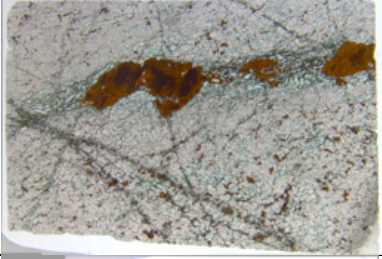
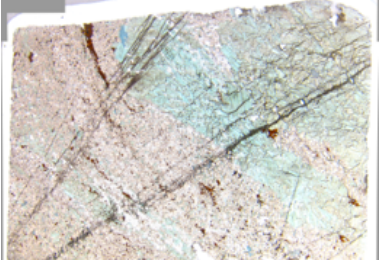
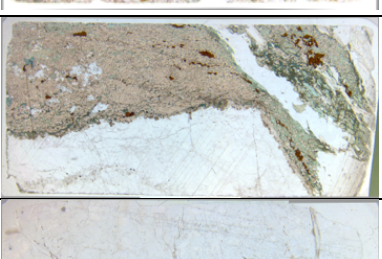
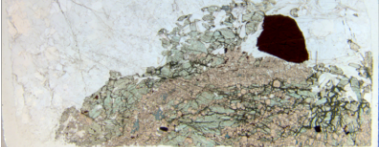
Large blocks of the Engebø eclogite (on a scale of several m² in outcrop) are often defined by parallel (up to 10 cm wide) bands of garnet (red bands) segregations that run at a strike

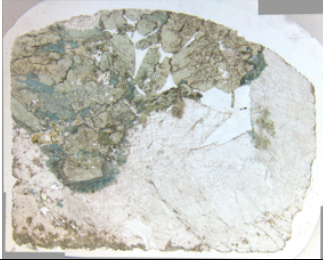
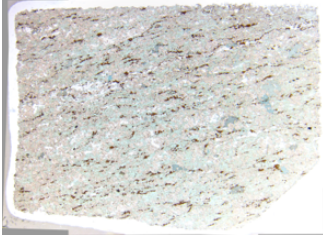
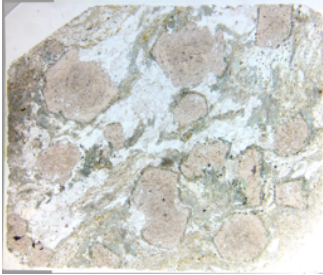
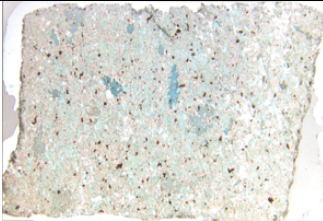

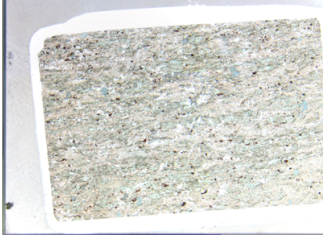

parallel to the east-west orientation (parallel to the Førdefjord) and keeps its parallel orientation for tens of meters along strike (fig.12a). Kleppe (2013) described observations of similar vein textures from outcrops at Engebøfjellet.

Folded zones at Engebøfjellet are abundant and are part of a set of structural markers that depicts a complex metamorphic history (Braathen et al., 2014). The shear sense on the Engebøfjellet are dominated by an E-W strike direction. Such a marker are seen in in fig.12c. Large rutile phenocrystals are usually not seen in quartz veins in the highly sheared zones. Highly sheared zones are most often associated with light colored eclogite, which was not analyzed in the field, but was interpreted to be leuco-eclogite. Observations lead to the impression that rocks that have a darker green-black and red color are generally less folded.

Table 5 give an overview of the thin sections produced and the general mineralogy and textures of the collected samples. In the following chapter, results relating to eclogite matrix textures, and vein textures are separated into two sub-chapters. The first part of this chapter presents the observations and analytical results for the eclogite matrix, that is, vein-unrelated eclogite. The following part presents all results obtained from vein textures.

Table 5: Thin section textures and general mineralogy. Mineral abbreviations after Whitney et al., (2010).

Sample	Thin section	Matrix description	Vein mineralogy
KGR4B			Large elongated omphacite crystals in quartz vein.
KGR4C1		Vein transitions into highly altered ferro eclogite matrix. Transition zone rich in; Omp, Symplectite. Also present; Py + Hem.	Quartz vein with large Rt w/ilm lamella. Omp are present. Mica are present at boundary with Rt crystal.
KGR4C2		Ferro eclogite matrix: Rt, Ilm, euhedral Grt, Omp, very little Amp.	Horizontal Omp rich vein, supported by a symplectite matrix. Vein hosts Rt with Ilm rims.
KGR4C3		Several veins cross cut each other. Large Rt are cross cut by thin veins. Matrix minerals are the same as in kgr4C2.	Large Rt in symplectite vein matrix. Omp + Rt show intergrowth as euhedral Omp crystals in Rt.
KGR5A1		A segregation of Omp rich, Rt free green area, and a Grt dominated red area with large elongated Rt clusters. Cut by later thin veins.	
KGR11		Matrix: Grt rich, with elongated clusters of Rt. Some Amp.	Zonation at eclogite boundary: Cal-Amp-Grt-Hem.
KGR12		Large amp porphyroblasts w/Grt overgrowth.	Quartz vein. Large Rt at boundary.

Sample	Thin section	Texture	Vein mineralogy
KGR13		Sample is from vein.	Calcite vein together with large segregation of Omp and Amp breakdown to Amp. Some quartz present.
KGR14		Grt, Omp, Rt + ilm. Abundant Qtz + Amp porphyroblasts with euhedral inclusions.	No veining
KGR15		Dominated by large euhedral garnet crystals with quartz tails. Garnets supported by Omp, Amp, Mica and Qtz. Garnets are inclusion rich and show internal deformation. Inclusions include Rt crystals.	No veins but texturally heterogenous compared to other samples.
KGR16		Large Omp crystals overgrowth of Rt + Grt. Amp overgrowth of Rt + Grt. Abundant Qtz.	
KGR17		Omp, Grt, Qtz, Rt, Ilm, Amp.	
KGR18		Foliated texture. Horizontal bands of fine grained symplectite, + elongated Omp and Qtz bands. Grt are fine grained. Also present; Amp porphyroblasts, Rt + lm.	
KGR19		Large euhedral garnets with abundant internal and external breakdown to Qtz. Matrix rich in Amp. Rt inclusions often seen in the garnets.	

5.2 Eclogite matrix

5.2.1 Eclogite petrography

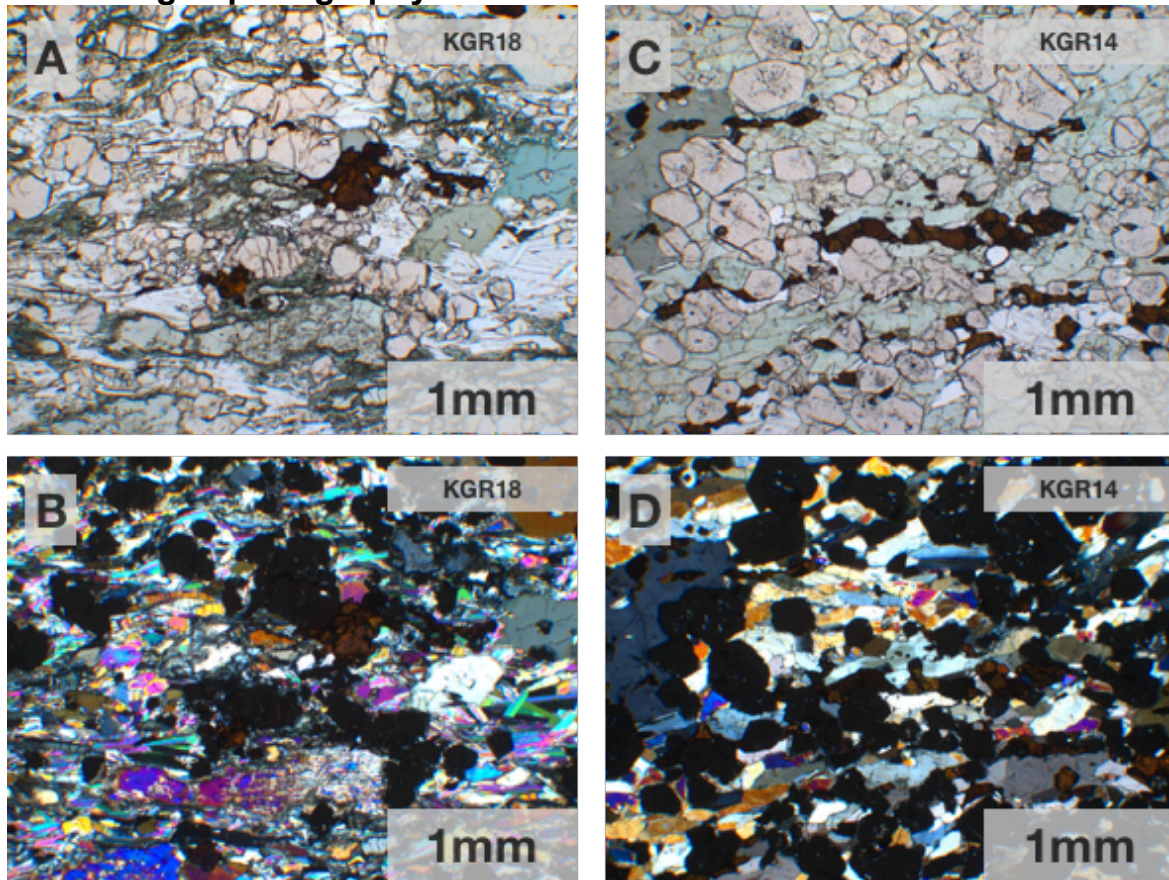


Figure 13. Texture comparison between leuco-eclogite (A+B) and ferro-eclogite (C+D). Photographs a+c are taken in plane polarized light. b+d are taken in cross polarized light.

The distinction between ferro and leuco-eclogite are made based on their chemical composition. The TiO_2 content are the defining property, where a content of 3% or more place the eclogite in the ferro category. Below 2% are leuco eclogite. Leuco eclogite have more abundant garnet breakdown to amphibole and quartz. Large garnets show internal deformation, and some leuco samples show rounded garnets surrounded by generations of smaller garnets which might indicate grain rotation during deformation. Quartz tails on garnets and elongated omphacite crystals are more prominent in leuco-eclogites. These textures are interpreted to form a tectonic fabric. Because they are oriented in the same direction. Thus leading to the interpretation that leuco-eclogite have suffered higher strain than the ferro-eclogite samples. This is also supported by previously mentioned observations of deformation in the field (see also fig.14). Another possible explanation is that leuco-eclogite have had lower rheological strength than the ferro-eclogite during deformation. This

can be explained by the overall garnet content compared to omphacite, which will influence the rheologic strength of the eclogite (Jin et al., 2001).

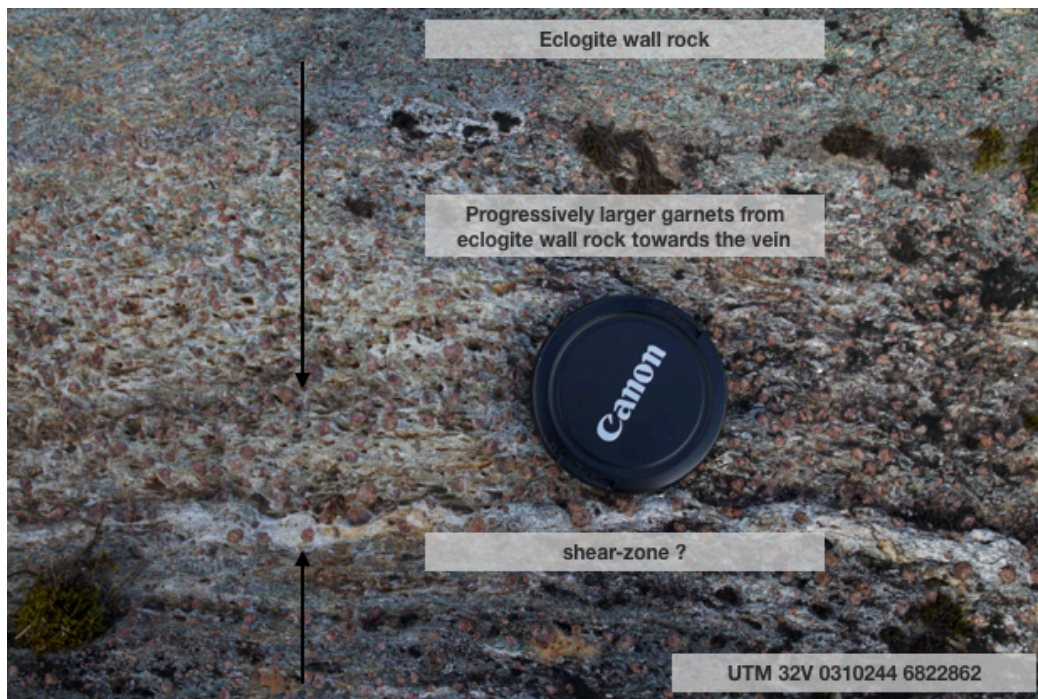


Figure 14. Leuco-eclogite vein / shear zone texture w/garnet.

Ferro-eclogite have mineral phases that are more well preserved. The crystal phases of garnet in particular are more euhedrally shaped in ferro-eclogite, and internal deformation along with crack propagation are less abundant in ferro garnets compared to their leuco-eclogite equivalents. Alteration or degradation from omphacite to symplectite and garnet to amphibole and quartz are less abundant in the ferro-eclogite matrixes. Unless such alteration is concentrated within veins. Symplectite are seen as dark green fine grained matrix in fig.13a and often supports elongated omphacite crystals.

5.2.1.1 Rutile

The TiO_2 content in the eclogite samples ranges from 1.5-5.5% across the analyzed samples (table.7). Microscopic and macroscopic observation place rutile in different settings and environments which could be related to different processes of deposition. Rutile occur in three texturally different settings, these are vein related rutile, inclusion related rutile and matrix rutile. The main type is matrix rutile which appear in equilibrium with the matrix forming minerals (fig.13c). The matrix rutile are often elongated and irregular, and together with omphacite form a foliated mineral texture in samples kgr14 and kgr18 (table.6). The total volume of inclusion rutile and vein rutile are not estimated. Based on observation it is the impression that these rutile textures are insignificant relative to the total volume of rutile

hosted as eclogite-matrix rutile. Vein rutile are discussed in the section about vein petrography.

5.2.1.2 Ilmenite

Ilmenite usually appear as an accessory phase in a close relation with rutile. It has been found in forms as lamellas in rutile (fig.32b), and often as rims around rutile. Its crystal habit varies between rounded and euhedral minerals in leuco-eclogite, but are more often observed as a breakdown product (retrogressive) in rutile with irregular crystal shapes. Ilmenite can be distinguished in reflected light microscopy, where the distinction between this phase and other opaque minerals can be seen more clearly than in transmitted polarized light. This can be seen in fig.29a.

5.2.1.3 Garnet

Garnets appear in various amounts in the eclogite samples. Garnets are together with omphacite the main matrix forming mineral in both ferro and leuco-eclogites at Engebøfjellet. The garnet crystals are generally euhedral. The grain sizes vary widely even within the same samples, and especially between some ferro and leuco samples, where leuco-eclogite have the largest garnets (sample kgr15 and kgr19 in table.5). Garnet breakdown to amphibole is observed at several locations in the eclogite matrix, but are more generally related with the contact zone between veins and matrix (figs. 20 and 21). Tiny inclusions of some unknown fluid or gas was observed within large garnets in leuco-eclogite sample kgr15 these was not investigated further because they only contained one phase and could therefore not be analyzed with microthermometry.

5.2.1.4 Omphacite

Omphacite is abundant on Engebøfjellet. In veins, observations of relict omphacites are seen as fine grained symplectite (i.e figs 27 and 29). Omphacite in the matrix appear to have an preferred main crystallographic axis that corresponds with the elongation in rutile. This could have been described using image analysis or EBSD maps with the SEM, but was not done for this thesis.

5.2.1.5 Amphibole

Amphibole are usually present either as porphyroblasts (fig. 15), showing overgrowth over garnet and rutile, or it is present as reaction rims formed around garnet (fig. 23).

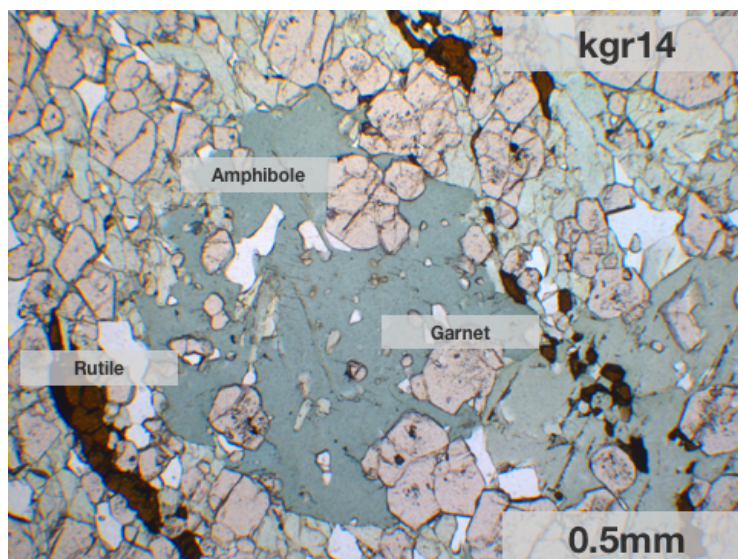


Figure 15. Amphibole porphyroblast in sample kgr14.

5.2.1.6 Pyrite and Hematite

Pyrite and hematite are only observed in veins textures, and are described in the following chapter about vein petrography.

5.2.2 Major element composition

Table 6. Major oxides analysis of eclogites from Engebøfjellet.

Sample	KGR 4C	KGR 4D	KGR 14	KGR 17	KGR 15	KGR 18	KGR 19
Type	Ferro eclogite	Ferro eclog	Ferro eclogite	Ferro eclogite	Leuco eclogite	Leuco eclogite	Leuco eclogite
Major elements (wt%)							
SiO ₂	42,22	42,41	44,22	44,38	40,24	48,21	42,55
Al ₂ O ₃	14,62	14,5	14,39	12,81	17,24	17,45	13,65
Fe ₂ O ₃ (T)	20,29	19,28	17,58	19,09	15,39	12,51	16,63
MnO	0,21	0,204	0,196	0,193	0,193	0,106	0,161
MgO	5,11	5,27	5,47	6,24	6,74	4,61	7,66
CaO	9,31	9,17	9,83	10,02	9,01	9,81	9,05
Na ₂ O	2,85	3,14	2,95	2,84	2,11	4,38	3,64
K ₂ O	0,08	0,04	0,05	0,04	1,18	0,41	0,17
TiO ₂	5,676	5,771	5,061	4,94	1,604	1,997	2,176
P ₂ O ₅	< 0.01	0,02	0,02	0,02	0,11	0,04	< 0.01
LOI	-0,36	-0,16	0,29	-0,21	6,25	0,73	3,76
Total	99,99	99,65	100,1	100,3	100,1	100,3	99,44

Ferro-eclogites have significantly higher amounts of iron, and less Al, Si, and K compared to leuco-eclogites. Two of the three leuco-eclogites show a loss of ignition of 6.25 wt.5 to 3,76 wt.%. The ferro-eclogites are characterized with none to very little loss on ignition.

5.2.3 Trace element composition

Table 7: Trace element compositions in ferro and leuco-eclogite samples from Engebøfjellet. < marks the element detection limit.

Sample	KGR 4C	KGR 4D	KGR 14	KGR 17	KGR 15	KGR 18	KGR 19
Type	Ferro eclogite	Ferro eclogite	Ferro eclogite	Ferro eclogite	Leuco eclogite	Leuco eclogite	Leuco eclogite
Trace elements (ppm)							
V	622	694	603	683	194	643	763
Cr	< 20	< 20	< 20	< 20	80	< 20	20
Co	89	114	63	70	38	59	81
Ni	< 20	< 20	< 20	< 20	90	70	120
Cu	30	10	50	20	40	50	40
Zn	120	110	110	130	70	90	110
Ga	18	19	18	21	15	22	15
Ge	1,9	1,5	1,5	1,6	2	1,5	1,4
As	< 5	< 5	< 5	< 5	< 5	< 5	< 5
Rb	< 1	< 1	< 1	< 1	31	6	< 1
Sr	30	26	96	53	238	284	66
Y	26,6	20,1	18,7	16,2	36,2	10,5	10,1
Zr	47	30	42	38	104	36	13
Nb	8,6	4,8	4	3,1	4,3	1,2	0,4
Mo	< 2	< 2	< 2	< 2	< 2	< 2	< 2
Ag	< 0.5	< 0.5	< 0.5	< 0.5	< 0.5	< 0.5	< 0.5
In	< 0.1	< 0.1	< 0.1	< 0.1	< 0.1	< 0.1	< 0.1
Sn	2	< 1	< 1	< 1	< 1	< 1	< 1
Sb	< 0.2	0,4	0,2	< 0.2	0,3	< 0.2	< 0.2
Cs	< 0.1	< 0.1	< 0.1	< 0.1	2,2	0,4	< 0.1
Ba	27	9	17	< 2	653	78	30
La	2,57	0,75	2,12	2,71	6,44	2,9	1,04
Ce	4,48	1,16	5,12	6,8	16,1	6,47	2,11
Pr	0,74	0,18	0,7	1,01	2,2	0,87	0,26
Nd	3,15	0,79	3,41	4,96	10,8	4,07	1,36
Sm	0,9	0,3	0,89	1,51	2,89	1,23	0,35
Eu	0,406	0,2	0,445	0,747	1,04	0,687	0,166
Gd	1,46	1,28	1,43	1,97	3,33	1,53	0,81
Tb	0,44	0,38	0,34	0,38	0,73	0,24	0,22
Dy	3,8	3,1	2,76	2,68	5,36	1,6	1,63
Ho	0,88	0,68	0,62	0,56	1,19	0,36	0,35
Er	2,67	1,96	1,85	1,56	3,43	1,09	0,97
Tm	0,425	0,289	0,28	0,227	0,502	0,153	0,135
Yb	2,91	1,91	1,79	1,51	3,29	1,02	0,84
Lu	0,456	0,302	0,28	0,237	0,5	0,166	0,129
Hf	1,5	0,9	1,4	1,2	2,4	1	0,5
Ta	0,78	0,46	0,35	0,23	0,2	0,07	< 0.01
W	1,8	1	< 0.5	0,7	79,5	< 0.5	1,2
Tl	< 0.05	< 0.05	< 0.05	< 0.05	< 0.05	< 0.05	< 0.05
Pb	< 5	< 5	< 5	< 5	< 5	< 5	< 5
Bi	< 0.1	< 0.1	< 0.1	< 0.1	< 0.1	< 0.1	< 0.1
Th	0,77	0,13	0,41	0,39	0,38	0,35	0,23
U	0,6	0,18	0,24	0,12	0,22	0,16	0,09

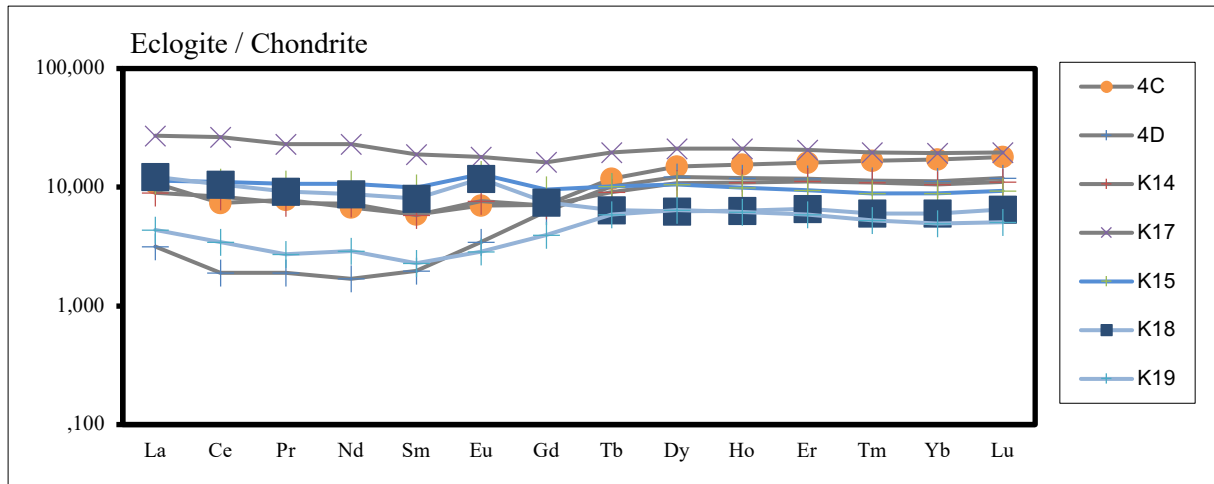


Figure 16. Eclogite samples normalized against chondrite.

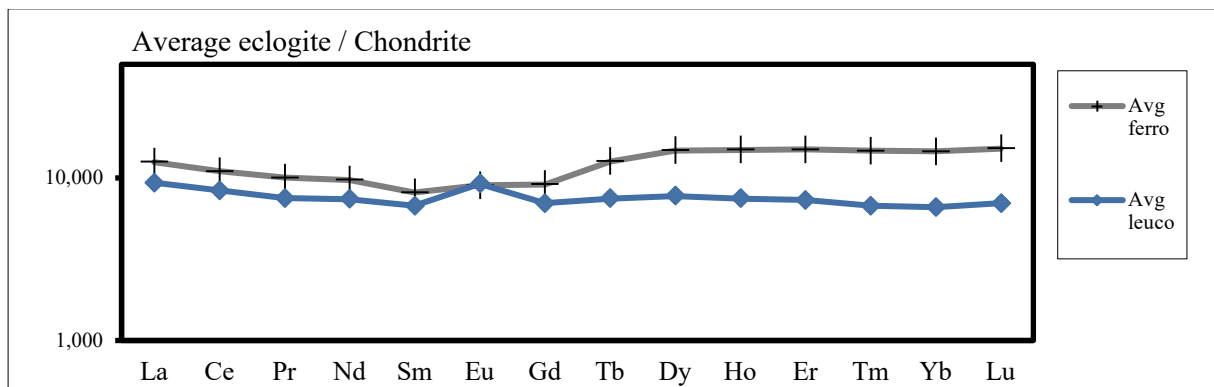


Figure 17. Average ferro and leuco-eclogite normalized against chondrite.

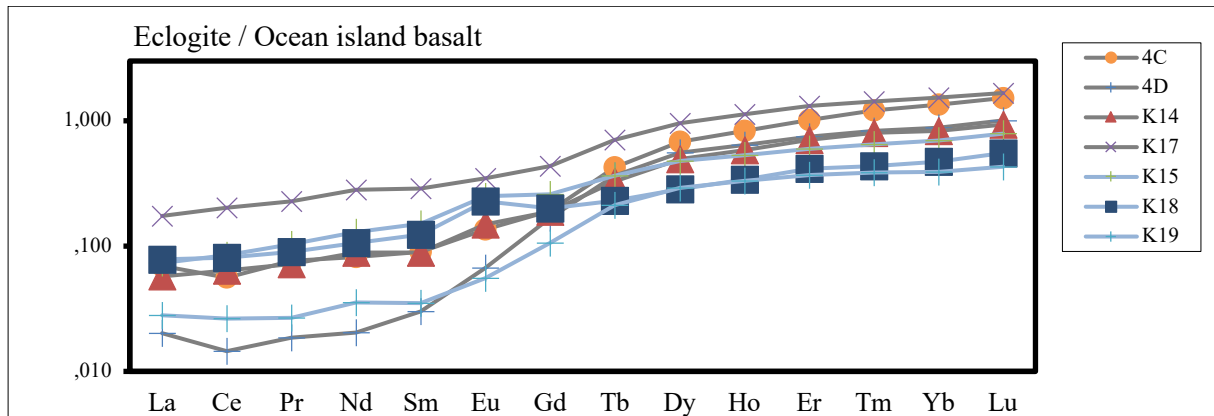


Figure 18. Eclogite samples normalized against ocean island basalt composition.

All seven eclogite samples were analyzed for their trace element compositions (table. 7). The REE values in the samples were normalized against chondrite and ocean island basalts values from Sun et al., (1989). We can see from these plots that average leuco-eclogite has a slight positive europium anomaly, and that ferro-eclogite samples generally are slightly more enriched in overall REE content compared to leuco-eclogite. The chondrite normalized REE curves show a relatively flat fractionation pattern for the eclogite samples which is more

typical of mid ocean ridge basalts rather than back-arc or ocean-island basalts (Sun et al., 1989).

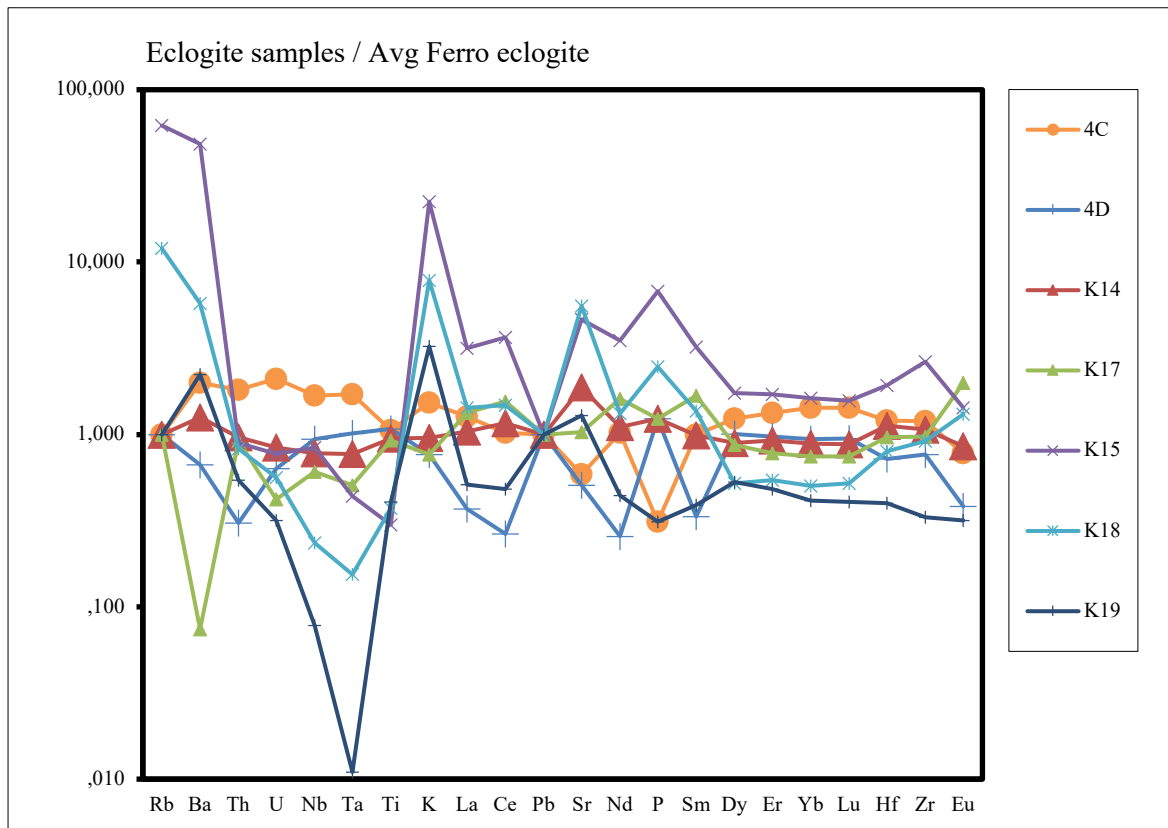


Figure 19. Multi element plot. All samples were normalized against the average ferro-eclogite composition. Kgr15, 18 and 19 are leuco-eclogite.

Figure.18 show the deviations in trace element compositions of samples compared to the average ferro-eclogite composition. Leuco-eclogite show the largest deviations which is most pronounced in Nb, Ta, Rb, Ba, Sr and K. The composition in each of the two groups of eclogite are not homogenous, leuco-eclogite can show relative enrichment in P in sample kgr15, and depletion in P in the leuco-eclogite kgr19. Leuco-eclogite kgr15 have a Nb and Ta content similar to average ferro-eclogite. Nb and Ta anomalies often follow the Ti content of rocks likely because these elements are compatible in rutile (Rudnick et al., 2010). The total TiO_2 content of leuco-eclogite sample kgr15 are less than half of the average ferro-eclogite TiO_2 content. This can imply that Nb and Ta can incorporate in significant amounts in some other mineral than rutile. On the other hand formation conditions such as oxygen fugacity (Liu et al., 2014) have been presented as one possible controlling factor for the partition of Nb into Rutile.

5.2.4 Spot analysis of rutile as inclusions within garnet.

Rutile was analyzed with the laser ablation method mentioned in the La-Icp-MS section.

Spot analysis of rutile inclusions in garnet are shown in fig.20.

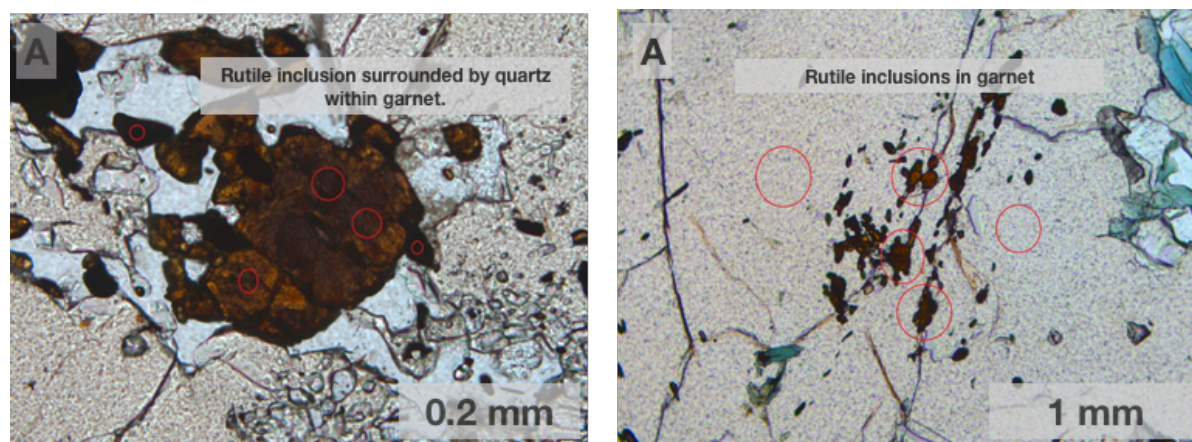


Fig 20. Sample kgr19. A: Rutile inclusion within garnet, surrounded by quartz. From leuco eclogite sample kgr19. Dark areas on the boundary zone of rutile represents breakdown to either ilmenite or titanite. B: Rutile inclusions in garnet.

Table 8. Trace element composition from rutile inclusions in garnet in leuco-eclogite sample kgr19 as seen in fig.20a. Numbers that are marked as below detection limit for la-icp-ms.

Spot size	Sample	Mg	Si	Ca	Mn	Fe	Cr	Zr	Hf	V	Nb	Ta	Sum REE
25m	19a3-rt25_1	795	2741	579	0,42	9565	40,13	51,18	2,7	4718	35,66	1,81	5,11145
25m	19a3-rt25_3	301	1896	118	0,385	2859	23,94	44,89	1,26	3558	23,09	0,822	0,6393
25m	19a3-rt25_4	693	3021	890	6,210	2962	35,4	44,46	2,81	3316	15,74	2,48	0,4748
25m	19a3-rt25_6	303	2310	950	2,650	1950	21,47	86,73	4,84	2979	19,77	1,2	0,42135
25m	19a3-rt25_8	473	5362	123	0,930	3870	16,69	5214	116,5	3127	17,77	1,11	6,82285

Table 9. Trace element composition from rutile and rutile-related inclusions in garnet in leuco-eclogite sample kgr19 as seen in fig.20b.

Spot size	Sample	Mg	Si	Ca	Mn	Fe	Cr	Zr	Hf	V	Nb	Ta	Sum REE
50m	19a1-rt1	3411	2293	5143	125	9263	9,68	64,73	2,55	3187	23,12	1,238	0,24671
50m	19a1-rt2	652	1930	453	11	4624	8	78,66	2,78	3035	22,11	0,698	0,28607
50m	19a1-rt3	3882	1979	6378	99	8488	7,46	62,49	2,08	3200	19,33	1,244	0,12446
50m	19a1-rt4	324	2053	25	1	3642	13,13	70,95	2,29	3031	21,45	0,934	0,17986
25m	19a1-rt25_4	297	2438	643	1	2477	24,85	50,67	1,92	3280	19,63	0,266	0,49195

5.2.5 Spot analysis of rutile and ilmenite in the eclogite matrix.

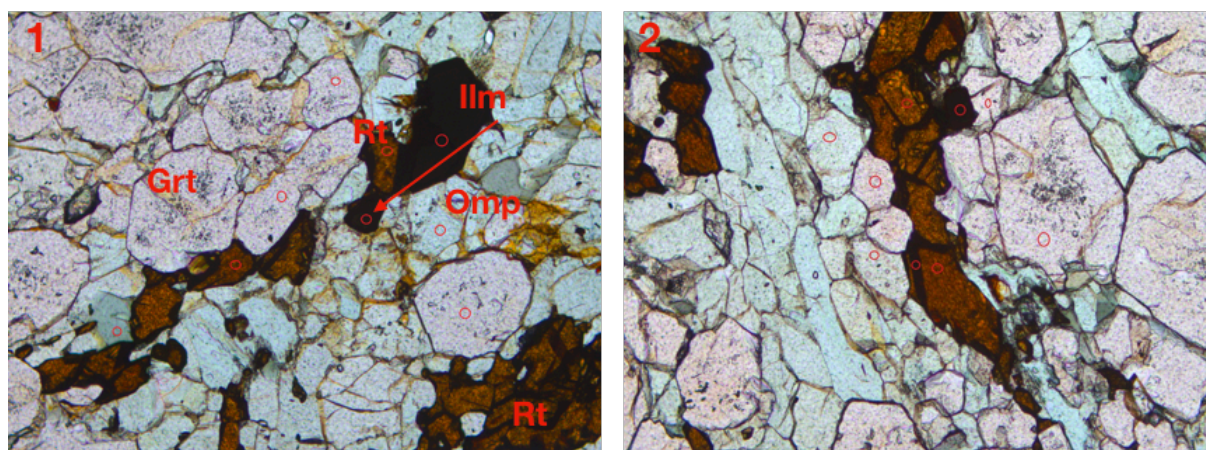


Figure 21. Rutile in ferro eclogite matrix from sample kgr4C2. Width of field for each photomicrograph is 3.3mm. Results from ablation can be seen in table 8.

Table 10. Trace elements in rutile from ferro-eclogite. Results are given in ppm. Numbers that are lined over are below detection limit.

Spot size	Sample	Mg	Si	Ca	Mn	Fe	Cr	Zr	Hf	V	Nb	Ta	Sum REE
50m	4c2a1-rt1	347	1932	30	0	3016	26,3	66,86	3,55	2433	242,3	15,31	0,21883
50m	4c2a1-rt2	2017	8153	1585	6	8445	27,7	67,01	3,36	2595	249,1	19,33	0,2267
50m	4c2a1-rt3	313	1996	29	0	4831	20,41	72,22	4,07	2529	227	18,45	0,11397
50m	4c2a1-rt4	1047	8152	526	84	9033	23,47	58,98	3,18	2391	214,4	15,98	1,2387
50m	4c2a2-rt1	329	2145	28	0	3743	27,9	78,7	3,81	2665	180,9	15,02	0,1303
50m	4c2a2-rt2	337	1980	24	1	3779	26,71	78,62	3,76	2765	214,3	17,14	0,1816
50m	4c2a2-rt3	335	1941	90	0	3803	31,83	78,4	3,83	2704	171,2	7,91	0,16053
50m	4c2a2-rt5	319	1874	25	0	3727	26,05	64,41	3,21	2424	144,8	7,21	0,1451

Table 11. Trace element composition from rutile and rutile-related inclusions in garnet in leuco-eclogite sample kgr19.

Spot Size	Sample	Mg	Si	Ca	Mn	Fe	Cr	Zr	Hf	V	Nb	Ta	Sum REE
50m	15a1-rt2	917	3984	1370	13	5960	289,9	4398	105,6	1716	254,3	11,47	18,173
50m	15a1-rt3	1320	2836	1601	20	5084	332,7	1182	32,71	1897	325,4	16,58	1,3979
25m	15a1-rt25_1	748	1943	619	5	3254	221,1	52,48	1,74	1747	264,5	12,61	0,432
25m	15a1-rt25_2	289	2025	94	2	3749	247,4	56,44	2,78	1829	295,3	20,22	0,5283
25m	15a1-rt25_3	322	2319	97	0	3294	235,8	60,69	3,22	1741	238,1	12,29	0,8355

Spot analysis of matrix rutile in ferro-eclogite samples (table.10) and leuco-eclogite samples (table.11) show Vanadium content in leuco-eclogite is lower overall compared to ferro-eclogite. Sample 15a1-rt2 and 15a1-rt3 have Zr values above 1000ppm and have also higher amounts of calcium and iron. The very high sum o REE in sample 15a1-rt2, is an outlier. This

sample also have higher than normal amounts of Zr and Hf. Sample 15a1-rt3 show similar behavior, although less pronounced.

5.2.6 Spot analysis of garnet and omphacite in ferro and leuco eclogite.

Garnet and omphacite from ferro and leuco-eclogite samples was ablated, results are shown in tables 12 and 13. In addition to the high field strength elements tables with the full range of elements analyzed are found in the appendix. The niobium and tantalum values in the garnet and omphacite was only detected at one instance, at values 0.01ppm for Nb, otherwise the values was below detection limit.

Garnet

Table 12. Trace element composition in addition to Fe, Ca and Mg for garnet in leuco-eclogite (kgr15 + kgr19) and in ferro-eclogite (kgr4C2). Numbers are given in ppm. Spot size was 50m. Underlined numbers are below detection limit.

Sample	Mg	Ca	Fe	Co	Ni	Cr	Ti	Zr	Hf	V	La	Lu	Sum REE
19a1-Grt1	11094	48173	156478	16,63	1,58	6,21	747,08	3,9	0,023	353,06	0,0046	2,159	20,492
19a1-Grt2	13808	47611	155444	19,79	1,15	8,33	662,31	1,396	0,015	432,78	0,027	1,096	15,537
19a1-Grt3	10839	46023	167856	16,01	0,99	5,88	793,93	1,581	0,0311	412,87	0	1,724	13,293
19a2-Grt1	20826	49878	161578	28,48	<u>0,116</u>	5,57	281,17	1,104	0,0396	218,22	0,0024	0,0554	6,8079
19a2-Grt2	14463	45075	171979	24,18	<u>0,1045</u>	3,33	362,75	1,421	<u>0,0057</u>	267,17	0,0046	0,1563	13,211
19a3-Grt1	19977	44218	190598	27,82	1,5	14,28	262,8	2,51	0,0842	180,85	0,002	0,396	18,302
19a3-Grt2	16225	44095	206291	21,24	0,75	11,94	338,73	1,275	0,0108	219,8	0,0033	0,239	12,358
15a1-Grt1	17952	64020	164335	55,54	0,274	5,03	595,18	1,69	0,0185	125,73	13,71	0,212	106,25
15a1-Grt2	22858	49991	166207	32,45	0,44	67,01	231,29	3,01	0,0112	78,21	0,001	0,1138	8,7585
4c2a1-Grt1	20106	52845	176874	63,23	<u>0,1315</u>	2,12	489,34	2,02	0,0316	49,77	0,0319	0,108	3,6773
4c2a1-Grt2	22303	53382	185645	70,6	<u>0,13</u>	7,88	1120,7	1,87	0,069	161,03	0,0117	0,715	19,495
4c2a1-Grt3	20251	56301	180849	62,54	<u>0,125</u>	1,79	700,21	2,68	0,0127	84,19	0,351	0,95	26,982
4c2a2-Grt1	22680	55350	195067	68,04	<u>0,135</u>	5,87	470,89	1,17	0,024	160,83	0,264	0,456	20
4c2a2-Grt2	24385	49015	199046	73,25	0,36	19,06	192,94	0,138	0,0213	443,32	0,0088	0,174	5,0722
4c2a2-Grt3	21379	60590	187134	66,95	1	5,94	167,95	0,734	0,0447	25,61	0,0399	0,176	7,3033

Ferro-eclogite garnets have higher amounts of magnesium, cobalt and generally slightly higher amounts of calcium and iron. There is no significant difference in the range of HFSE and REE. One major drawback to this data is that zonation in garnet was unfortunately not considered while planning the spots for ablation. In fig.21 red circles mark the points for ablation. Sometimes these are placed in the center and at other times closer to the boundaries of garnets. This makes the detailed comparison less usable. Because zonations from core to rim can reflect changing metamorphic or fluid conditions during crystal growth.

Omphacite

Table 13. Trace element composition in addition to Fe, Ca and Mg for omphacite in leuco-eclogite (kgr 15 + kgr19) and in ferro-eclogite (kgr4C2). Numbers are given in ppm. Spot size was 50 μ m. Underlined numbers are bellow detection limit.

Sample	Mg	Ca	Fe	Co	Ni	Cr	Ti	Zr	Hf	V	La	Lu	sum REE
19a2-omp1	80907	47247	74087	62,16	275,78	9,61	1585,8	2,45	0,208	997,35	<u>0,0017</u>	0,0019	0,7565
19a2-omp2	79738	43554	76723	59,41	252,37	5,98	1141,6	1,755	0,18	891,61	0,0054	0,0074	0,5188
19a2-omp3	81718	48807	82337	67,65	264,36	7,73	2087,9	2,28	0,949	982,03	0,0146	<u>0,00107</u>	1,4019
19a3-omp1	79562	41409	78126	78,57	271,04	16,5	1052,9	1,77	0,131	746,41	<u>0,00103</u>	0,0008	0,3438
19a3-omp2	82236	47618	86534	82,69	302,65	6,56	1501,3	2,04	0,185	784,96	0,001	0,0029	0,6824
19a3-omp3	83947	57004	96446	87,38	298,13	9,54	2118	3,38	0,273	772,29	0,0167	0,0021	1,9919
15a1-omp2	76282	38892	73113	77,53	559,79	110,6	965,09	1,49	0,0688	291,77	0,0019	0,0083	1,2107
4c2a2-omp1	41325	80728	47692	26,84	12,3	8,89	389,83	1,26	0,193	650,07	0,0033	<u>0,0014</u>	0,0965
4c2a2-omp2	45114	89551	44337	22,63	10,2	8,98	377,73	1,41	0,216	671,68	<u>0,002</u>	0,002	0,1349
4c2a1-omp1	46752	88578	41949	46,69	21,72	6,81	426,39	1,94	0,245	695,65	0,006	<u>0,0011</u>	0,4002

From this limited dataset, omphacite have significantly lower contents of magnesium, iron, cobalt, nickel and titanium in the three ferro-eclogite samples compared to leuco-eclogite. Calcium content is higher in the three ferro-eclogite samples. The content of high field strength elements does not show any significant difference. Vanadium content is overall slightly higher in the leuco-eclogite sample compared to ferro-eclogite samples.

5.3 Eclogite veins

5.3.1 Vein petrography

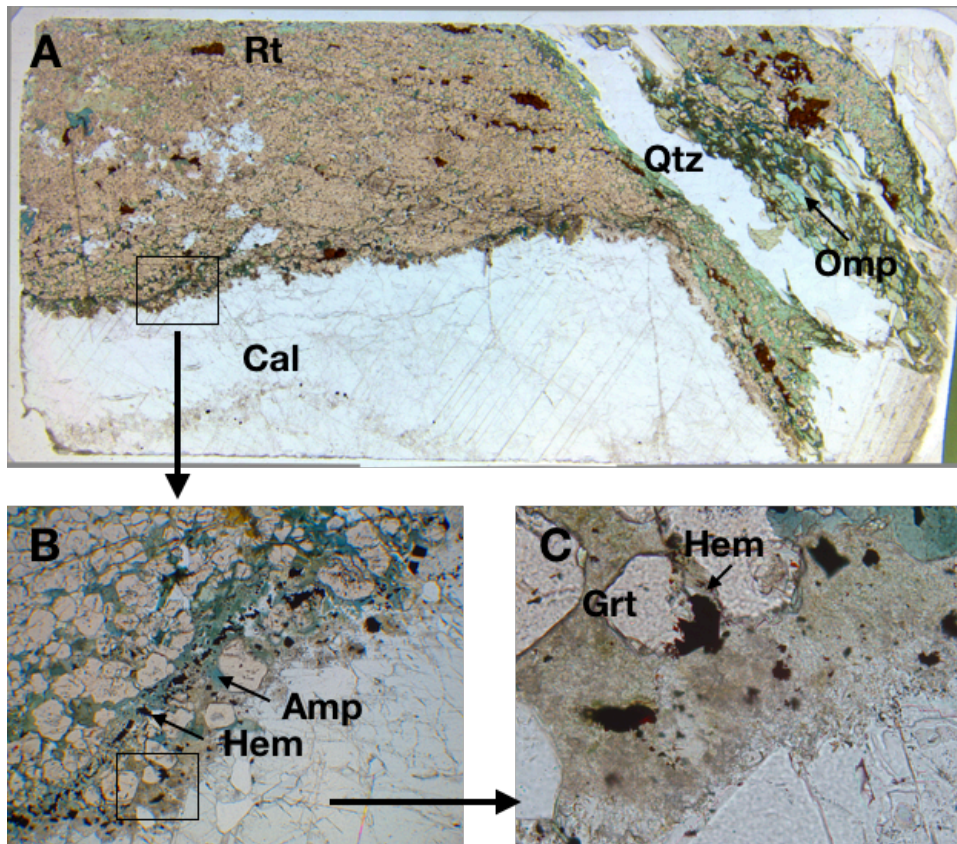


Figure 22. Width of fields; A: 4 cm, B: 3.3 mm, C: 0.7mm, all images are seen in plane polarized light. A: Carbonate vein from drill core sample KGR11 are shown. The boundary between eclogite (red and green area) and calcite vein show zonation that are evident around the entire rim of the calcite. B: show a section of this zonation pattern. The boundary with eclogite are marked with a line of black/opaque hematites. Amphibole rims (green-blue color) are seen around garnet. C: The relationship and intergrowth of a garnet together with hematite. Mineral abbreviations after Whitney et al., (2010).

5.3.2 Carbonate in veins

Carbonate are present as large segregations in some veins and are accompanied by deposition of hematite and garnet breakdown to amphibole fig.22. Carbonate appear as pods or segregations with sharp boundaries to other vein minerals such as omphacite and quartz. Rutile was never observed within carbonate vein material. Sometimes omphacite are seen to fill cracks within carbonate (fig.27). The garnet to hematite transition in figs 22c and 23, is untypical, but is included because it seems like the outer angle of the hematite are inhering the garnets crystal phases.

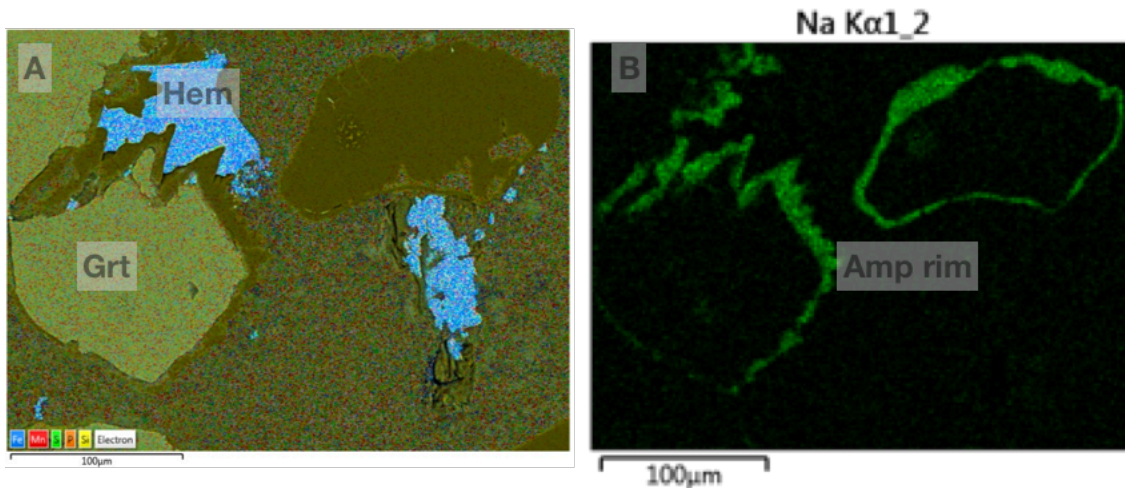


Figure 23. A: EDS map of garnet to hematite breakdown. B: All other elements than Na are blacked out from the map, showing clearly the formation of a Na rich amphibole rim around the garnet.

5.3.3 Omphacite in veins

When omphacite occurs in quartz veins it often is present as euhedral, elongated crystals. At the contact zone between vein and eclogitic wall rock, an omphacite rim is always present in the quartz vein samples (fig.24). This feature is however not present at vein-carbonate contacts. Omphacite at these rims have textures that resembles free-growth in an aqueous medium.

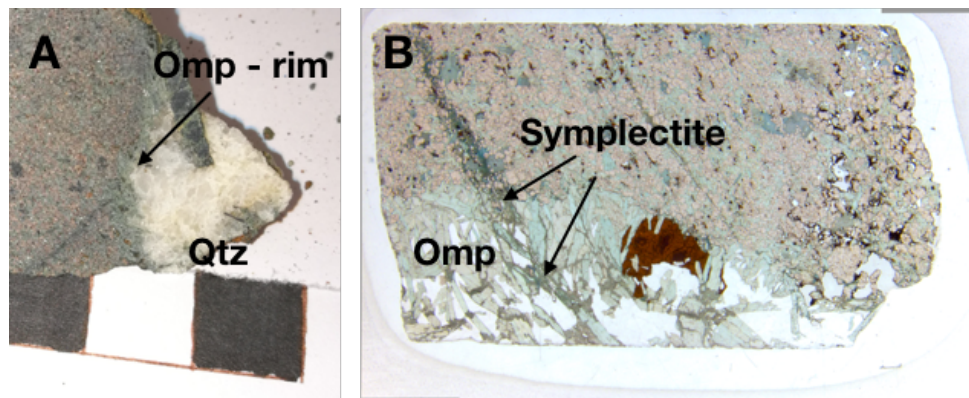


Figure 24. Figure a and b show the transition from ferro-eclogite to quartz veins, and the fibrous elongated omphacite crystals that are present at this interface. B. Elongated omphacite crystals show intergrowth with a large (3-4mm) rutile phenocrystal (brown). Symplectite are seen as dark, fine grained material together with omphacite.

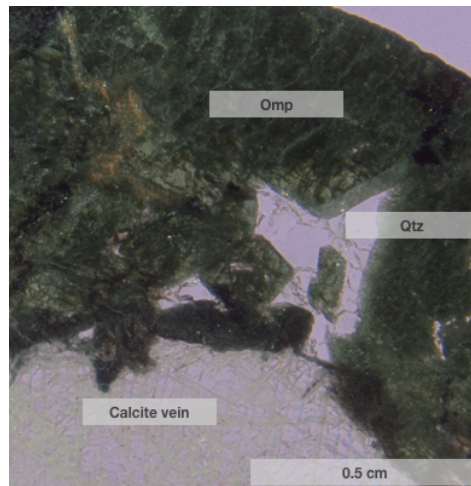


Figure 25. Sample kgr13. Vein calcite in contact with omphacite and quartz

Calcite is often present together with omphacite and quartz. Omphacite can form solid solution between diopside and Jadeite ($\text{CaMgSi}_2\text{O}_6 - \text{NaAlSi}_2\text{O}_6$) (Liu., 1980). The relationships seen in fig.24 can be simplified to only account for the diopside component in omphacite and modelled with an reaction of the form $\text{CaMg}(\text{CO}_3)_2 + 2 \text{SiO}_2 \leftrightarrow \text{CaMgSiO}_6 + \text{CO}_2$ (Luth 1995). The addition of CO_2 to the system could explain the growth of calcite and quartz in the vicinity of diopside-omphacite. No fluid inclusions was found in the quartz domain seen in fig.24.

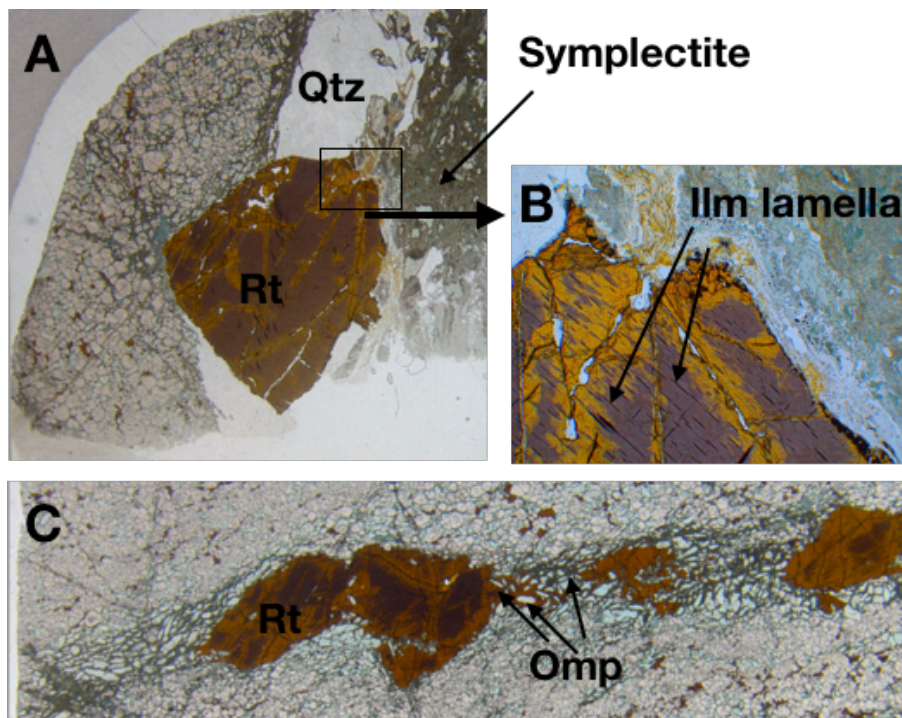


Figure 26. A; photomicrograph width approximately 1.5 cm, large rutile in a quartz omphacite vein in ferroeclogite matrix. B: Width of photomicrograph 3.3 mm. C: Large rutile segregations in a vein type consisting of symplectite and elongated omphacite, with of section, approximately 2.5 cm.

5.3.4 Rutile

Rutile are observed in omphacite and quartz dominated veins in scales ranging from mm thin segregations to large veins at meter scale in the field. Rutile often show intergrowth with elongated omphacite crystals (figs. 24 and 26c). Rutile are most often found along the contact with wall rock. Rutile found in veins are regularly seen together with pyrite and hematite (fig.27).

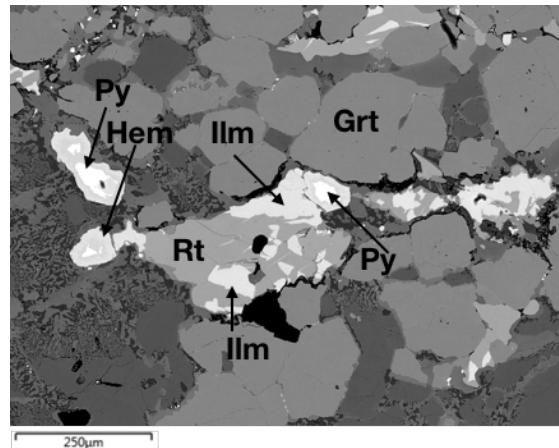


Figure 27. Rutile, ilmenite, pyrite and hematite cluster within symplectite vein of sample KGR4C1, Surrounded by euhedral garnet.

5.3.5 Garnet

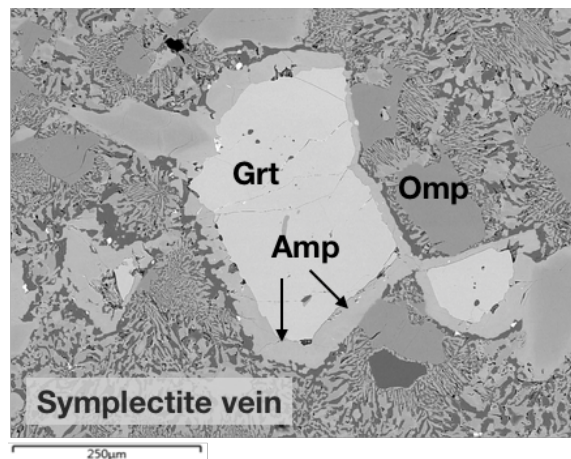


Figure 28. Garnet breakdown to amphibole are clearly seen in this BSE image. The selected area is otherwise dominated by omphacite and symplectite.

Garnet in omphacite-symplectite veins usually show breakdown to amphibole along its rim, this is seen in the backscattered electron image (BSE) (fig. 28). This feature is also seen in carbonate veins, where garnet breakdown is present at the wall rock contact zone (fig. 23).

5.3.6 Pyrite.

Pyrite is not a major constituent in the veins, but it is often found together with ilmenite, rutile and hematite (figs. 29 and 30). Pyrite breakdown to hematite is observed in samples at several locations in the ferro-eclogite symplectite-veins. Pyrite is quite difficult to distinguish from ilmenite in cross and plane transmitted polarized light and are best seen with the reflected light microscope, as seen in fig.29A, and confirmed with EDS map in fig.29b. The breakdown of pyrite to hematite in a fluid as shown in fig. 30 would involve the release of H⁺ ion to the solution and thereby decreasing the pH of the fluid.

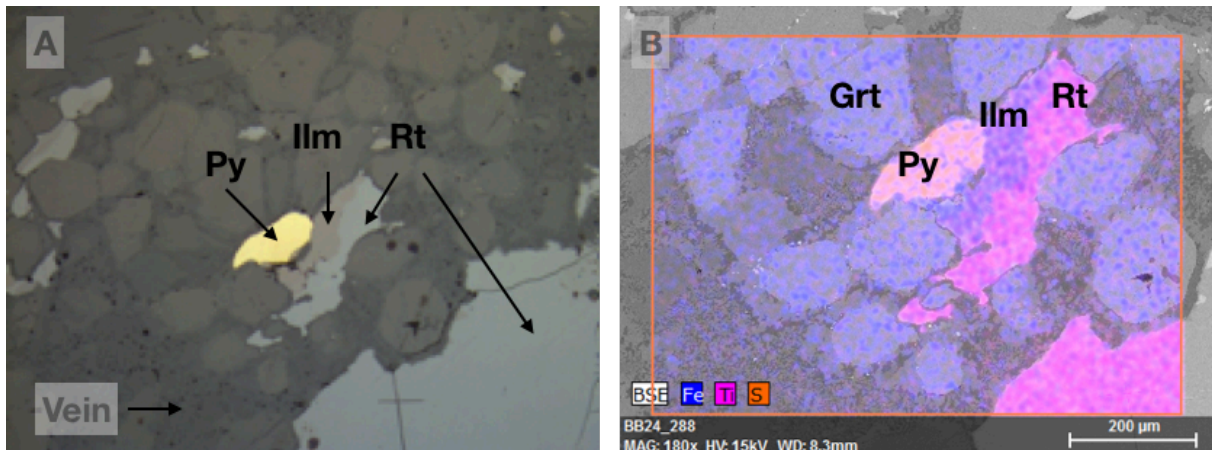


Figure 29. Rutile, Ilmenite and Rutile seen in reflected polarized light , and in a EDS map calibrated to show S= Yellow, Fe = Blue, Ti = pink.

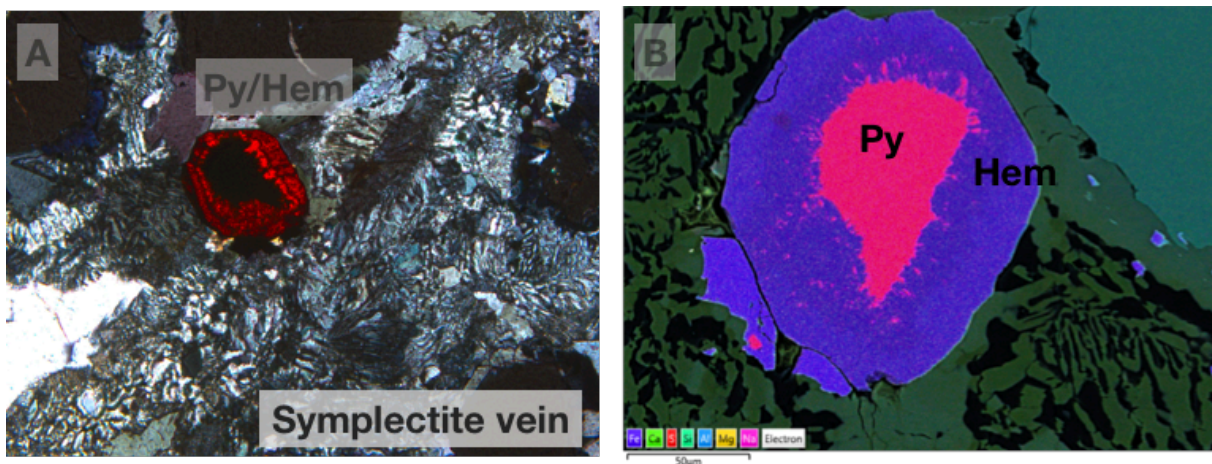


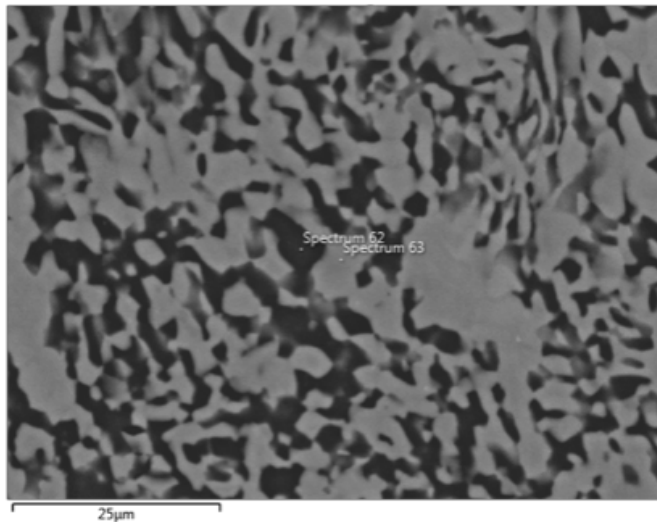
Figure 30. A: Pyrite breakdown to hematite (vivid red rim) are seen in cross polarized light. Width of photomicrograph is 0.7mm. B: This mineral breakdown was investigated with an EDS map to confirm the mineralogy.

5.3.7 Ilmenite

Ilmenite is present as a breakdown product around rutile in some veins. Ilmenite lamella are observed within the large rutile crystals in fig.32, these lamellas was ablated and their composition are shown in tables 14-15. The breakdown reaction of rutile to ilmenite involves the consumption of O and Fe.

5.3.8 Symplectite.

Symplectite in ferro-eclogite veins are abundant and are interpreted as a breakdown product of omphacite because the gradient between omphacite and symplectite in SEM was gradual without sharp contacts. The symplectite composition was analysed using the EDS detector. The dark component seen in fig. 31, consists of an albite like mineral. A suitable mineral phase for the light-coloured part of the symplectite was not found, its chemical composition in wt.% are shown in fig.31.



Spot 63	
Element	Wt.%
O	41,8
Si	26
Ca	14,7
Mg	6,9
Fe	6,5
Al	2,1
Na	1,8

Spot 62	
Element	Wt.%
O	47,0
Si	32,0
Al	11,0
Na	7,7
Ca	1,4

Figure 31. Sample kgr4C3. Symplectite with major element wt.% given in tables. Spot 63 = light mineral. Spot 62 = dark mineral.

5.4 Trace element composition of vein minerals.

Selected rutile and ilmenite minerals from thin sections was analyzed using the LA-ICP-MS method. Two rutile phenocrystals were found in the field in larger vein systems, these was analyzed using the litho geochemistry method. Carbonate from three drillcore samples was also analyzed for its trace element composition.

5.4.1 Rutile and ilmenite trace element composition

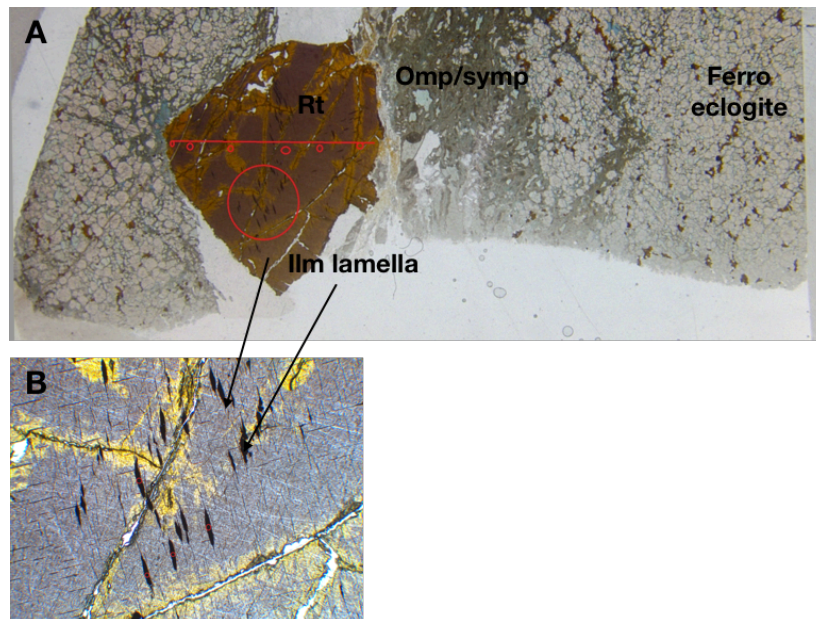


Figure 32. Red circles mark areas that was analysed with the ablation method. Sample KGR 4C1, vein from ferro eclogite. A: Overview of large rutile phenocrystal. B: Ilmenite lamella seen within the phenocrystal. Results are listed in table 14 and 15.

Table 14 . Rutile trace element composition from vein rutile in sample kgr4C1. Numbers in cursive and bold are below detection limit.

Spot size	Sample	Mg	Si	Ca	Mn	Fe	Cr	Zr	Hf	V	Nb	Ta	Sum REE
50m	4c1-rt1	324	2189	22	0	6572	13,04	62,36	3,57	2514	178,4	18,15	0,10463
50m	4c1-rt2	329	2148	24	0	6866	16,5	67,23	4,13	2657	205,8	20,93	0,142
50m	4c1-rt3	328	1974	26	0	11426	16,72	67,61	3,8	2495	192,1	21,27	0,16442
50m	4c1-rt4	346	2024	27	1	7427	14,86	64,42	3,98	2535	197,2	19,59	0,19125
50m	4c1-rt5	339	2021	25	0	5185	15,47	65,38	3,63	2504	189,3	19,8	0,18962
50m	4c1-rt6	352	2053	161	0	7433	15,32	68,02	3,77	2681	197	19,73	0,2005
50m	4c1-rt7	339	2096	85	1	6462	14,95	58,21	3,19	2385	205,4	25,43	0,20501
50m	4c1-rt8	344	2104	23	1	7367	16,26	59,67	3,53	2492	205,7	25,46	0,16624
50m	4c1-rt9	335	1960	127	0	6381	11,03	61,3	3,81	2599	207,5	26,81	0,21342
25m	4c1-rt25_1	322	3345	107	1	5851	22,08	66,58	4,14	2319	189,7	24,37	0,5305
25m	4c1-rt25_2	335	2949	818	2	5469	28,04	77,68	3,68	2513	211,1	26,11	0,62485
25m	4c1-rt25_3	289	1657	102	2	4635	25,44	67,74	3,41	2258	174,2	22,84	0,44545
25m	4c1-rt25_4	280	1950	102	0	11238	5,53	67,23	4,21	2375	203,8	25,29	0,4241

Table 15. Ilmenite lamella in rutile sample kgr 4C1. All numbers in ppm. Marked out numbers are bellow detection limit.

Spot size	Sample	Mg	Si	Ca	Mn	Fe	Cr	Zr	Hf	V	Nb	Ta	Sum REE
25m	4c1ilm1	5741	2165	123	157	339712	15,41	3,04	0,87	1976	11,71	7,89	0,48285
25m	4c1ilm2	5985	3032	155	2171	344480	23,7	3,22	0,423	2112	14,66	7	0,4801
25m	4c1ilm3	5320	8818	167	2108	330783	16,59	5,61	0,92	1985	27,65	10,68	0,3494
25m	4c1ilm4	5771	3430	390	164	355743	1,885	2,02	0,69	2118	11,97	6,87	0,61625

The high field strength elements Zr, Hf, Nb and Ta have higher concentrations in rutile compared to ilmenite. Ilmenite contains Mn, very little Mn are recorded in the rutile samples.

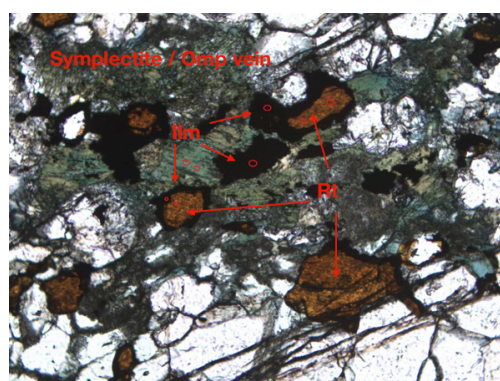


Figure 26. Ilmenite or Titanite rim (black) around rutile (brown). From vein segregation in sample kgr4C2 (ferro eclogite). Width of field for photomicrograph 1.8 mm.

Table 16: Vein rutile from sample kgr4C2. All numbers in ppm.

Spot size	Sample	Mg	Si	Ca	Mn	Fe	Cr	Zr	Hf	V	Nb	Ta	Sum REE
50m	4c2a3-rt1	330	2055	25	0	2256	31,08	86,44	4,16	2496	174,1	6,39	0,20238
50m	4c2a3-rt2	327	1809	23	2	2681	27,56	52,85	3,3	2733	157,4	12,22	0,16981
50m	4c2a3-rt3	330	1643	26	4	2617	28,73	71,09	3,84	2970	199,4	14,47	0,15988

Lithochemochemistry of large rutile phenocrystals.

In addition to spot analysis using the ablation method, two large rutile phenocrystals was analyzed using the lithochemochemistry method. All REE except Ce was bellow detection limits and therefore they are not included in the table. Th is also bellow detection limit.

Table 17: Trace element composition of large rutile phenocrystals found in the field. Numbers in ppm.

Sample	Type	Ni	Cr	Zr	Hf	V	Nb	Ta	U
KGR 2C	Rutile in Qtz vein	240	< 20	58	3,3	1880	42,4	4,19	1,27
KGR 3	Rutile in Omp vein	240	30	61	3,5	1540	56,8	4,66	0,35

5.4.2 Trace element composition of carbonate.

Most elements in the carbonate analysis show concentrations below detection limit. Only the elements Sr, Zn, Co, Pb and Ba show any enrichment above detection limit.

Table 18. Trace element composition of carbonate from veins. All numbers in parts per million. <, marks detection limit.

Sample	Type	Sr	Zn	Co	Pb	Ba
KGR 11	Carbonate	1550	130	27	6	< 3
KGR 15	Carbonate	529	50	19	6	5
KGR 13	Carbonate	1810	110	49	11	12

5.5 Stable isotopes

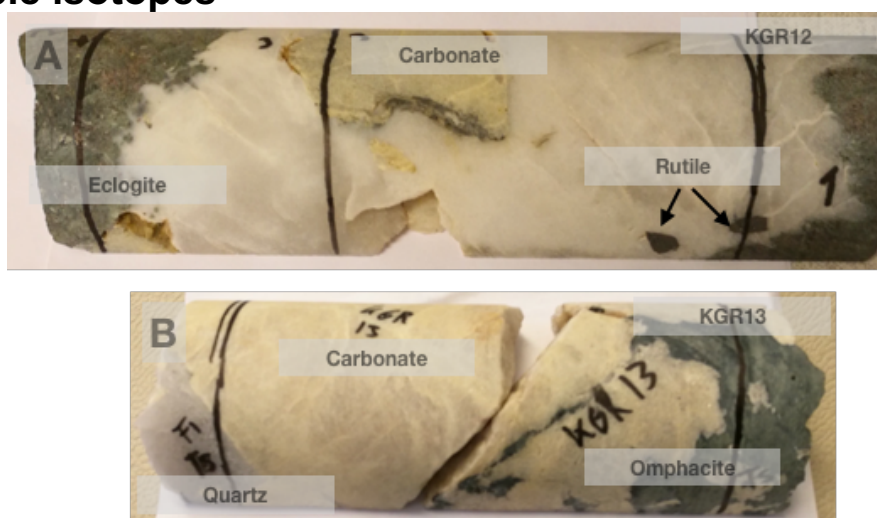


Figure 27. Textural relationships between Calcite, quartz and omphacite.

Table 19. Oxygen and carbon stable isotope composition of three carbonate veins in the Engebøfjellet eclogite.

Sample	11A	11A - dup	11B	11B - replica	11B - dup	13A	13A - dup	13B	13B - dup	15A	15A - dup	15B	15B - dup
$\delta^{13}\text{C}$ VPDB [‰]	-6,08	-5,99	-6,06	-6,04	-6,03	-6,22	-6,14	-6,34	-6,28	-6,86	-6,95	-6,89	-6,91
$\delta^{18}\text{O}$ SMOW [‰]	9,32	9,36	9,33	9,27	9,30	9,17	9,21	9,15	9,10	8,92	8,87	8,92	8,91

The $\delta^{13}\text{C}$ and $\delta^{18}\text{O}$ stable isotope composition was reported in the VPDB standard. The $\delta^{18}\text{O}$ values was recalculated to the SMOW standard using the formula $((1.03086 * \delta^{18}\text{O}_{\text{vpdb}}) + 30.86)$. The results (table.19) are consistent and show very little variation between sample locations. Samples was taken from different depths in the deposit and was spaced up to 100 meters apart (table.3).

5.6 Fluid inclusions

For this study the objective was to produce fluid inclusion data from as many different vein textures as possible, approximately 15 samples were prepared. One carbonate vein from sample KGR11 and, and quartz vein material in 4D5 and 4D11 was analyzed (fig. 33). The most fine grained quartz samples from shear zone quartzs as described in the field work section, did not show inclusions that was suitable for microthermometry. Either because they was too small or did not contain more than one phase.

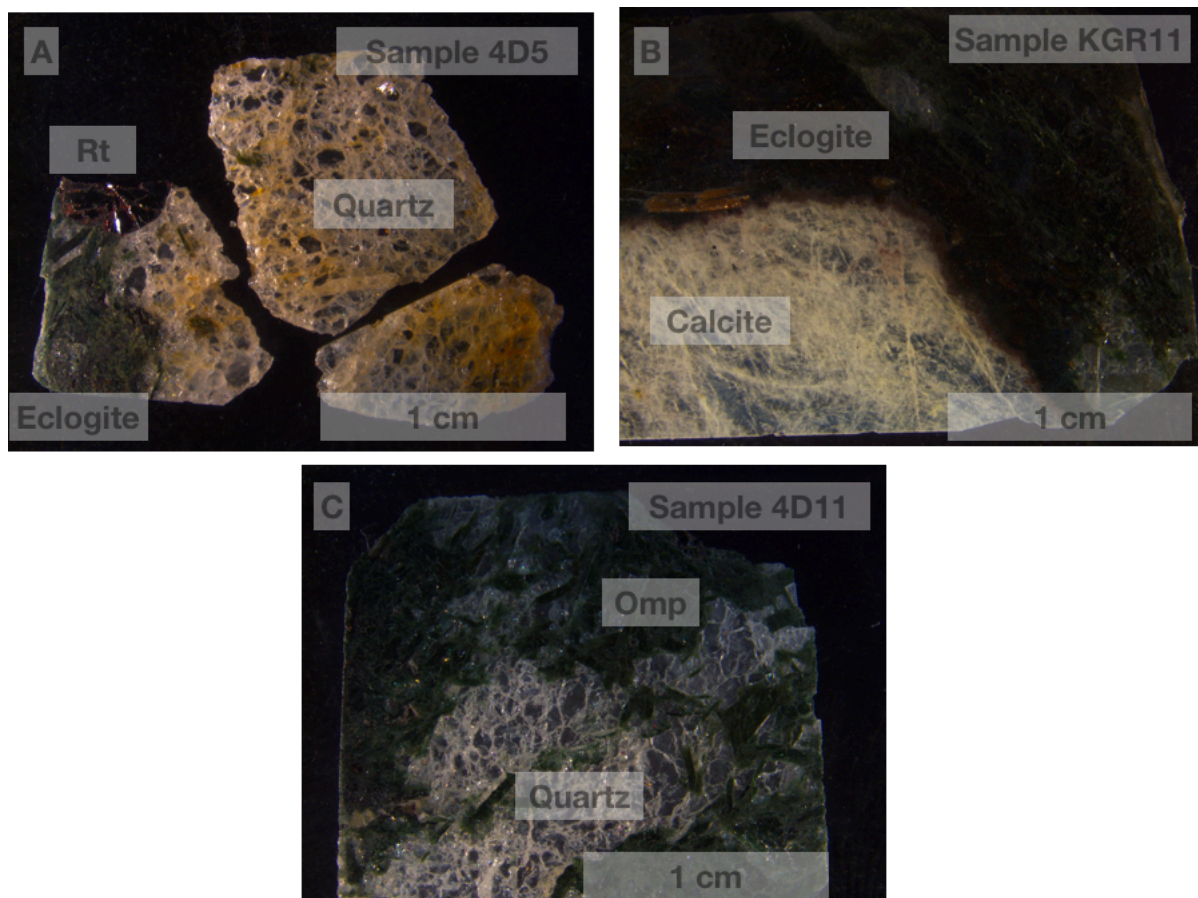


Figure 33: Overview of analyzed samples for fluid inclusions. The only sample that was directly associated with rutile precipitation was sample 4D5.

Fluid inclusions categorization.

The fluid inclusions have been grouped in four groups based on number of present phases at room temperature, and based on the calculation method used. Not all salinities and isochores was calculated using the same procedure, it is therefore important to clarify which method was applied to which specific group of inclusions. **Category A** was two phase inclusions with $H_2O(l)$ and $CO_2(g)$. **Category B** was polyphase inclusions with $H_2O(l)$, $CO_2(g)$ and halite (or equivalent) daughter crystals. **Category C** with $H_2O(l) + CO_2(l) + CO_2(g)$. For category c inclusions, the total homogenization temperature was not recorded so it was not possible to

produce density estimate and isochore for this group. **Category D** inclusions consisted of H₂O(l) + CO₂(g) inclusions where the homogenization temperature of CO₂ was not recorded. As introduced in the theory chapter, the CO₂ homogenization temperature should be included to estimate salinity from clathrate melting. Since this was not recorded, the method after Bozzo et al., (1975) was used. This method is described in the theory chapter.

Eutectic temperatures.

The eutectic temperatures for sample 4D11 and sample 11 was similar, sample 4D5 show lower eutectic temperatures (Table 20).

Table 20. Average and median eutectic temperatures in °C for the measured samples. N = number of measurements.

	Mineralogy	Te (average)	Te (median)	n
Sample 4D5	Qtz	-37,4	-37,3	19
Sample 4D11	Qtz	-51,5	-51,4	14
Sample 11	Cal	-52,6	-53,0	24

Table 21. Relationship between eutectic temperatures and composition of fluid inclusions. (modified after Shepherd et al., 1985).

Salt system	Eutectic Temperature C (Te)
H ₂ O-NaCl-CaCl ₂	-55
H ₂ O-MgCl ₂ -CaCl ₂	-52,2
H ₂ O-KCl-CaCl ₂	-50,5
H ₂ O-CaCl ₂	-49,5
H ₂ O-Na ₂ CO ₃ -K ₂ CO ₃	-37
H ₂ O-NaCl-FeCl ₂	-37

Comparison of eutectic temperatures found for this thesis with table.17 after Shepherd et al., (1985) give fluid composition with a high content of CaCl₂. Melting temperatures in sample 4D5 correlate to a Na₂CO₃-K₂CO₃ component or a NaCl-FeCl₂ component of its fluid.

5.6.1 Fluid salinity

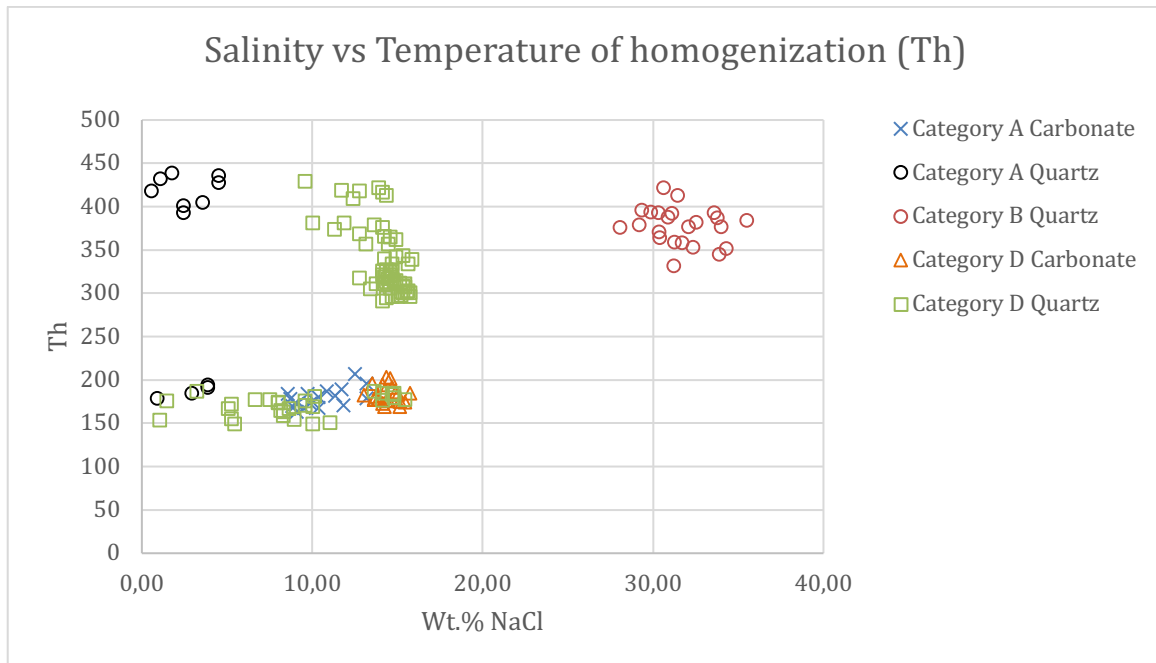


Figure 34. Salinity vs Temperature of homogenization (Th) for recorded inclusions.

Carbonate inclusions show less variability and occupy a smaller area of the diagram (blue and orange markers) compared to the quartz inclusions (fig.34). Quartz inclusions (green markers) overlap the same field as carbonate inclusions.

Table 22. Median and average Wt.% NaCl equivalent for each group of fluid inclusions and for all inclusions.

Samples	Median Wt.% NaCl	Average Wt.% NaCl
Class A	8,68	6,72
Class B	33,39	34,08
Class C	5,77	6,78
Class D	14,33	13,15
All samples	14,33	16,30

Table 23. Median and average Wt.% NaCl equivalents for all recorded inclusions in each sample.

Sample	Median wt.% NaCl	Average wt.% NaCl	Mineralogy
4D5	14,44	12,53	Quartz
4D11	30,307	23,49	Quartz
Kgr11	10,36	10,50	Carbonate

Table 22 show the salinity estimates for the inclusions based on the categorization that was presented at the start of this chapter. In table 23 the salinity is sorted based on sample. Fluid inclusions in sample 4D5 have a lower salinity than inclusions in the quartz-omphacite vein in

the sample 4D11 (fig.34). Halite crystals was not observed in the 4D5 sample, while this was present in abundance in the 4D11 sample. Rutile was present as a vein precipitate in sample 4D5. Rutile was not present in the omphacite rich 4D11 vein sample, with higher salinities. The inclusions in carbonate sample kgr11 have an lower salinity. All salinities for 4D5 inclusions was calculated with the use of the formula after Bozzo et al., (1975).

5.6.2 Fluid inclusion isochores

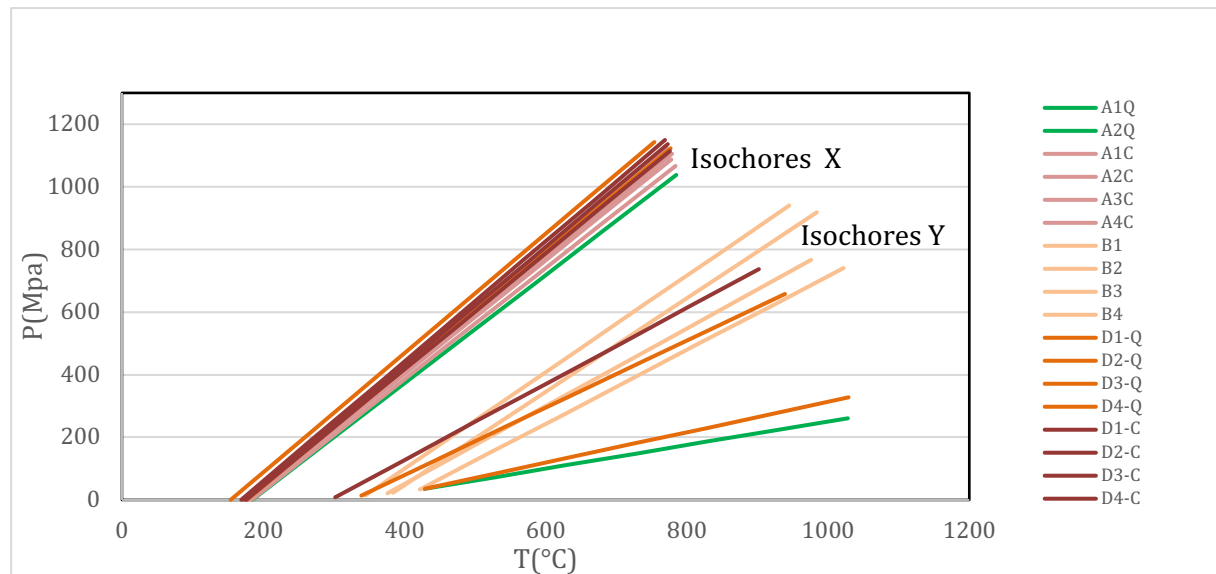


Figure 35. Fluid inclusion isochores. Suffix-C means that the inclusion was found in carbonate, Q means it was found in quartz.

Fluid inclusion isochores was produced for category a, b and d inclusions. These are visualized in fig.35. Because category-C did not include total homogenization temperatures, the isochores could not be produced for these inclusions. Most inclusions are grouped in the set of isochores labelled “isochores X”. The set of isochores labelled “isochores Y” represent the high salinity category-B inclusions found in quartz, additionally one carbonate inclusion and one quartz inclusion from the category-D are found in this set of inclusions. Four isochores was selected for each group and each mineralogy based on the following criteria: One high density inclusion, one low density inclusion, one high salinity inclusion and one low salinity inclusion. This was selected to represent the range of possible isochores for each group of inclusions.

6 Discussion

6.1 Geochemistry.

The major geochemical characteristic of the two rock types in terms of major elemental composition is a higher amount of iron and titanium in ferro-eclogites. The leuco-eclogites exhibit the most Al and K.

Trace element composition of ferro and leuco-eclogite show some characteristical differences. Although it should be noted that only seven samples in total, and only 3 samples for the leuco-eclogites should not be considered representative for the entire deposit. Fig.35 show selected trace element compositions of the eclogites. Kgr 15, 18 and 19 are leuco-eclogites. Some trends are definitive, as the tantalum and niobium depletion in leuco-eclogites which are believed to be attributed to the preferential incorporation of these elements in rutile. This relationship has previously been discussed by Rudnick et al., (2000).

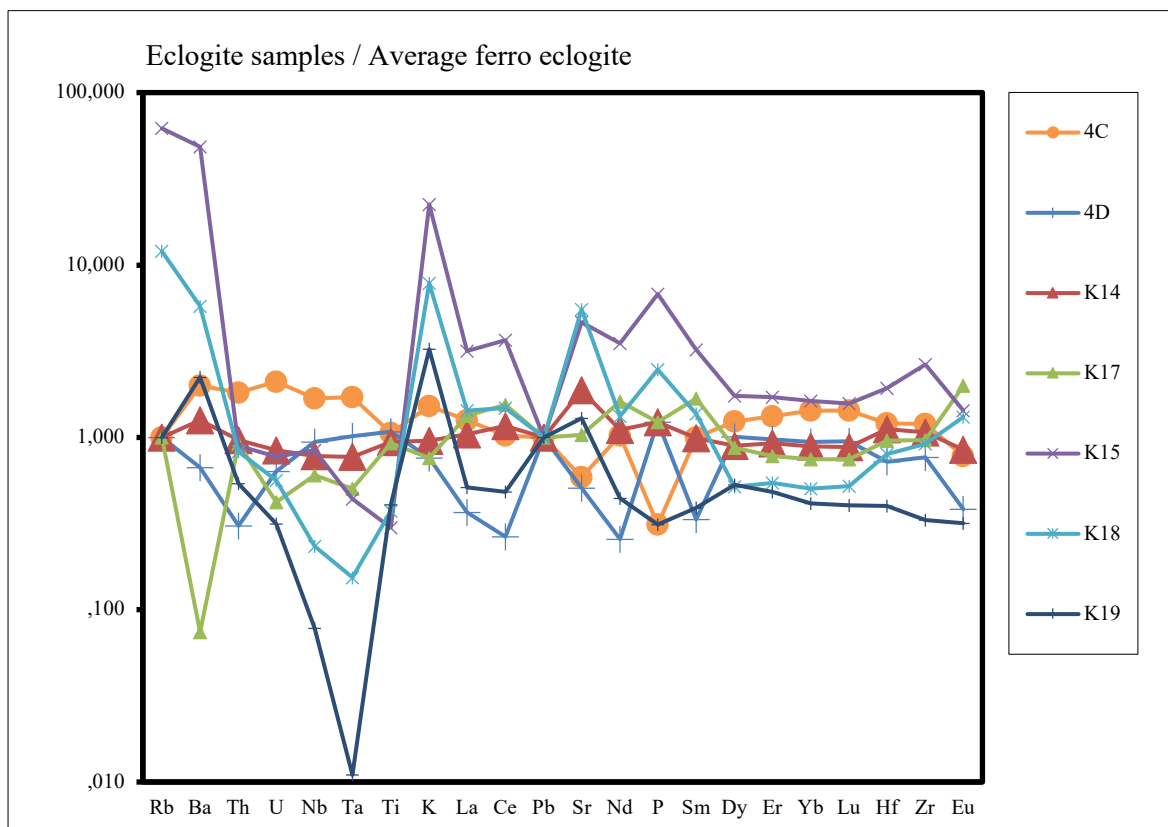


Figure 36: Trace element composition of Engebø eclogite samples normalized against average ferro-eclogite composition.

Interpretation of REE and trace element patterns in ferro and leuco-eclogite rocks.

The REE composition indicate that the eclogite is more similar to a tholeiitic morb than an ocean island basalt type protolith. The La to Lu are gradually more compatible, the slope of these elements can therefore be used to interpret the degree of fractionation in a magma. The last melt to crystallize from a magma should have a relatively high amount of the LREE compared to the HREE (McSween et al., 2003). This is because as the magma crystallize the compatible HREE have a higher preference to enter the crystal lattice of the minerals than the LREE.

All the eclogite samples are more depleted in the light rare earth elements (LREE) than the Heavy rare earth elements in the Ocean island basalt diagram. Compared to Chondrite, the REE patterns are relatively flat for both types of eclogite. This leads to the interpretation that the Engebø eclogite have originated from an unmodified mantle source, similar to MORB rather than a more modified OIB setting (Sun et al., 1989).

The lanthanoids (REE) elements (except Eu and Ce) have 3+ charge. Ce can have its charge altered to 4+ in an oxygen rich environment, whereas the Eu can have its charge altered to 2+ in an reductive environment. These two elements therefore do not fractionate in the same ordered way as the REE elements with 3+ charge. Eu with a 2+ charge will show exchange with the calcium ion. Calcium rich minerals such as plagioclase can be a sink for Eu²⁺. The REE compositions of eclogites in the western gneiss region have previously been studied by Gebauer et al., (1985). These authors found that some eclogites (with probable gabbroic origin) in the Selje region (north west of the Engebøfjellet) had a positive Eu anomaly. This anomaly was explained by magmatic fractionation of plagioclase rich magma under low-P conditions.

Gebauer et al., (1985) also discussed the probable source region of the eclogite protoliths based on the range of REE patterns found in the different eclogite locations of their studied area. Because of the heterogeneous REE patterns found in the eclogites, the source region was interpreted as a back-arc or island-arc signature rather than mid ocean ridge setting. The authors also briefly discussed whether the eclogite had acted as an open or closed system during eclogitization, at the time no evidence on REE mobilization during eclogitization existed. The contrasting Eu behavior in the samples was used to argue against secondary

alteration of the REE patterns in the eclogite.

An alternative explanation for the relative enrichment of HREE in some of the eclogite samples could be Wt.% garnet. Garnet show preferential incorporation of HREE over LREE. HREE are more compatible in garnet compared to omphacite (fig.36).

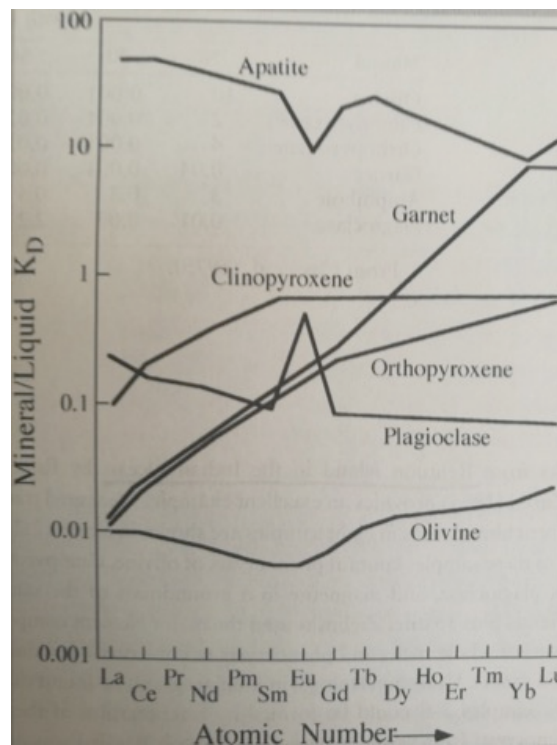


Figure 37. REE compatibility ($K_d > 1$) from liquid to Garnet and Clinopyroxene. After McSween et al., (2003).

6.2 Trace element behaviour in texturally different rutile

Three types of texturally different rutile were observed in the eclogite samples. Rutile was found as inclusions within garnet, as matrix forming minerals in textural equilibrium with the rock forming minerals and as large phenocrystals in veins. Matrix forming rutile was analysed in both ferro and leuco-eclogite, vein rutile was found in veins that was situated within ferro-eclogite and the inclusion rutile within garnet was only analysed in leuco-eclogite.

Vanadium and Niobium content in rutile.

Vanadium and niobium have been proposed by Liu et al., (2014) to be competitive in their incorporation to rutile. Both V and Nb substitute for Ti which usually have a charge of 4+ (fig.37) (Meinhold 2010). Niobium normally have a 5+ charge, and vanadium have a 3+ charge. Under conditions of decreasing fO_2 , there will be more available V^{4+} and this will compete with the Nb^{5+} for the available spots in the rutile crystal lattice (Liu et al., (2014).

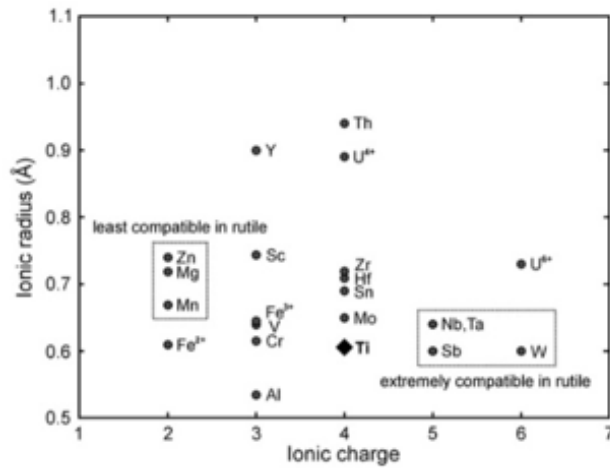


Figure 38. Ionic radius vs ionic charge for elements that readily incorporate into rutile. After Shanon (1976) in Meinhold (2010).

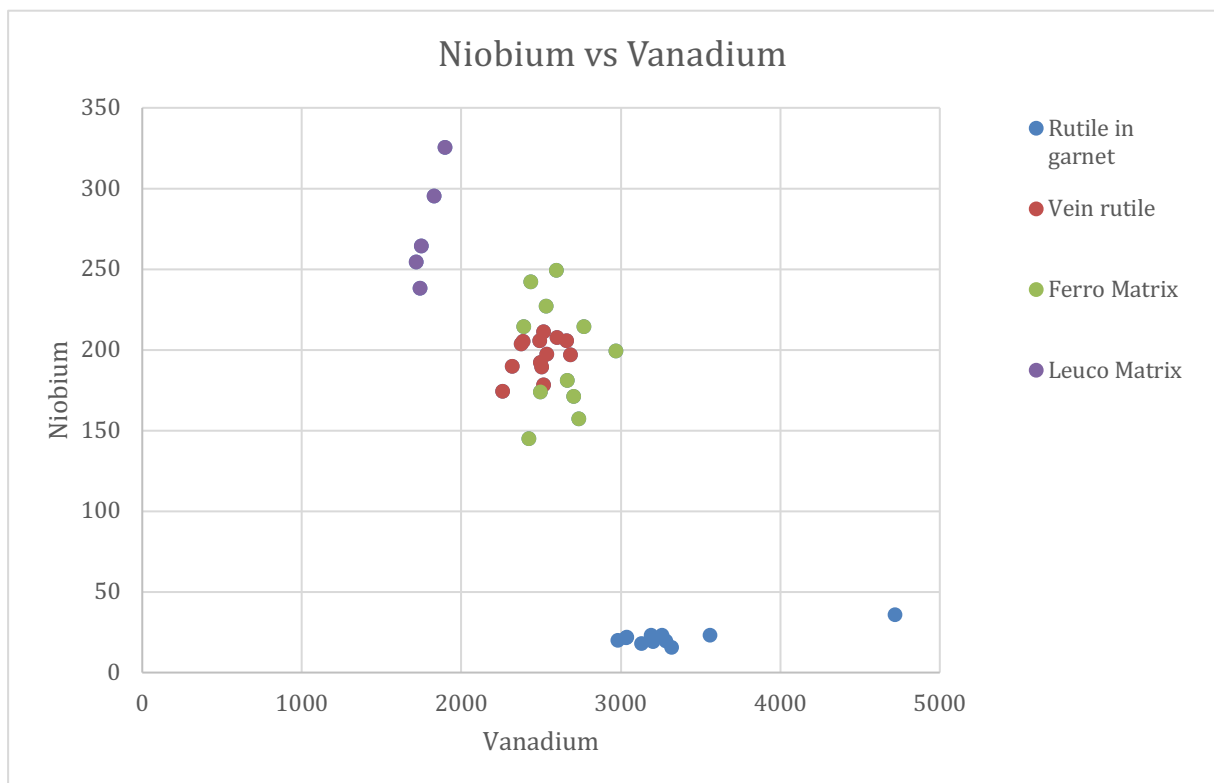


Figure 39. Rutile from Engebø samples analyzed with the LA-ICP-MS method.

The relationship between Nb and V in rutile from the samples in this thesis is shown in fig.38. There is a somewhat negative correlation between Nb content and V content (fig.22), although most samples plotted in an random cluster in the middle of the diagram.

Interestingly, the relationships between V and Nb reflect their depositional environment. Nb content in rutile that was encapsulated within garnet was significantly lower than Nb content in the leuco eclogite matrix. Rutile from ferro-eclogite matrix are grouped together with the vein rutile. The similarity between the V and Nb trace element composition of rutile in veins

in ferro-eclogite and the matrix rutile in ferro-eclogite can indicate that the vein rutile is sourced from the same rock type. Ti, V and Nb have similar chemical properties and we can perhaps extrapolate that these elements are mobilized in the same way. We can therefore speculate that these elements will partition equally in contact with a fluid, and that the content of V in Nb in vein rutile reflect the content in the fluids. According to the theory by Lui et al., (2014), the leuco-eclogite rutile should have encountered a higher fO_2 during recrystallization, compared to garnet-inclusion rutile.

Niobium behavior in a rutile with ilmenite lamella.

The large rutile phenocrystal in sample krg4C1 was ablated in spots that aimed to represent pure rutile, and ilmenite lamella spots. The Nb content in the 11 rutile spots show a high consistency, with concentrations between 174 ppm and 211 ppm. The niobium content of the ilmenite lamella within rutile show Nb values between 11-27 ppm (4 spots). These measurements can give indications about the affinity of Nb in rutile compared to Ilmenite. We already know that Nb substitute for the Ti element at the Ti site in the rutile crystal lattice. The relative importance of the Ti sites in ilmenite ($FeTiO_3$) are (1/5) compared to (1/3) in rutile TiO_2 . If we assume that the rutile and ilmenite equilibrated under the same P-T conditions, the content of Nb in ilmenite should be limited by the availability of Ti sites in ilmenite. The relative availability of Ti sites in ilmenite are 60% of that of rutile. But the observed partition results in ilmenite represent far less than 60% of the Nb content found in rutile.

Uranium content in rutile

Uranium content in rutile varies significantly between ferro and leuco-eclogite samples. From well under 1 ppm in most rutile analysed in leuco-eclogite, to values between 2-3ppm in ferro eclogite samples. Uranium content in rutile from the literature varies between 0.01 and 170 ppm, as summarized by Meinhold (2010).

The closure temperature of U in Rt have been studied because of its significance to U-Pb dating. The different U content in rutile could be explained by different cooling histories of the rocks. The closing temperature of U in rutile are also strongly dependent on grain size (Meinhold 2010). Grain sizes of inclusion rutile in garnet of the leuco-eclogite samples are much smaller than the matrix rutile found in ferro.

6.3 Fluid characteristics.

P-T conditions of veins.

In order to adhere to Roedders rules (Bodnar 2003a), fluid inclusions should have had a constant and unchanged chemical composition and volume since they were entrapped. However, an internal overpressure of 1Kbar is sufficient to decrepitate inclusions larger than ca. 15µm in quartz (Andersen et al., 1989). Decrepitation of fluid inclusions can be recognized by looking at the phase relationship between multiple phases in a set of inclusions. The phase relationship should be relatively constant in a set of inclusions that have not suffered decrepitation. Also, the shape of the inclusions can be used, where necking down can be seen as star shaped inclusions, where fluids have propagated outward at weak points in the inclusion (Shepherd et al., 1985). Shear forces and deformation will accelerate this type of decrepitation of inclusions (Andersen et al., 1989). No two phase or polyphase inclusions were observed in samples from shear zones, or from larger quartz veins. This is interpreted to be related to decrepitation and recrystallization of inclusions in this environment

The occurrence of primary inclusions entrapped at peak metamorphic conditions was discussed by Van den Kerkhof et al., (2013). They state that primary inclusions are unlikely to have survived peak metamorphic conditions for high grade rocks. The samples investigated in this study contained primary inclusions without reported signs of decrepitation. This point towards the interpretation that the fluids originated and were trapped in the inclusions after peak metamorphism. The timing of the fluid phases is therefore believed to be placed somewhere along the retrogressive exhumation path and not the progressive metamorphic path.

Braathen et al., (2014) modelled the exhumation path of the Engebøfjellet eclogite. This path is used as pressure correction for the isochore data that was calculated from the salinity, density and homogenization temperature data of the fluid inclusions samples in this thesis (fig.40). The exhumation starts with a steep incline and loss of pressure before it slopes more gently and loses temperature. Two lines were drawn to represent the upper, and lower limit of the recorded temperatures that were presented in table. 24 after Braathen et al., (2014).

Table 24: Exhumation path data for the Engebøfjellet eclogite. After Braathen et al., (2014).

Metamorphic stage		Pressure (Mpa)	Temp C
Eclogite facies	D1+D2	1550-1800	600
Garnet amphibolite facies	D3	800	525-540
Epidote amphibolite facies	D4	700-800	500-525
Greenschist facies fracturing.	D5	300-400	300

Isochores that were calculated show large variability but are generally grouped in two main groups. This reflects the grouping also seen in the salinity vs Th diagram (fig.33). The fluid inclusion isochores does not cross the exhumation path after Braathen et al., (2014). The exhumation path starts to change its slope at the D3 point (fig.40), which marks the garnet amphibolite facies. The slope of the main group of isochores are quite similar to the slope of the exhumation path from the D3 to D5 stage. This leads to the interpretation that fluids represented by these isochores could have been entrapped at this late path, and therefore is to be considered late retrogressive fluids.

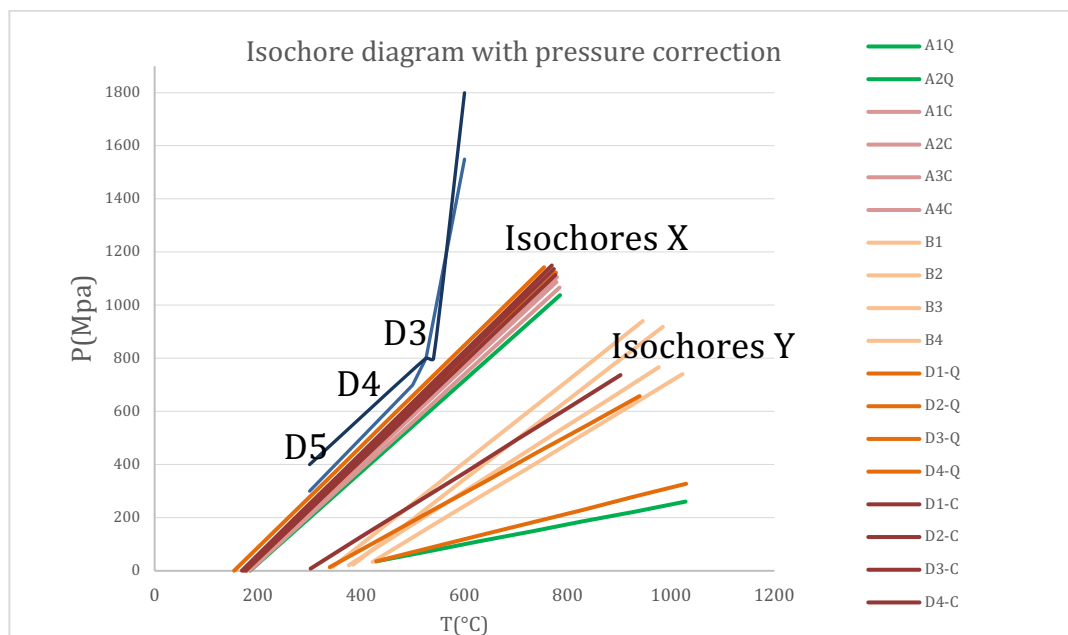


Figure 40. Lines of pressure correction (blue) with calculated isochores.

Textural observation of garnet breakdown to amphibole at the contact with carbonate vein in sample kgr11 supports the placement of fluid inclusions represented by isochores X entrainment close to the retrograde amphibole facies path. The other group of isochores Y and the outliers beneath this group are harder to place in the tectonic framework. One explanation for these inclusions can be post entrainment changes during metamorphism. This group of inclusions are dominated by the category-B inclusions. Category-B inclusions have the

highest salinity recordings (average 34 wt.% NaCl). Could the high salinity in this group have been caused by loss of liquid from post entrapment leaking from the inclusion during deformation? Leaking of fluids could perhaps alter the phase relationship in the fluid inclusion and increase the salinity of the residual liquid.

Fluid salinity.

Inclusions that are most closely related to rutile deposition have an average salinity of 12.5 wt.% NaCl (sample 4D5) (table.22) In sample 4D11 quartz and omphacite seemed to show growth in the same fluid, supported by the observation of elongated, randomly oriented omphacite. Sample 4D11 was characterized with high salinity inclusions with halite daughter minerals. The average salinity for these inclusions was 23.49 wt.% NaCl (high salinity category-B inclusions was part of this sample). The high salinity 4D11 sample did however not come with precipitation of rutile phenocrystals. Sample KGR11 show inclusions from carbonate that was related with breakdown of garnet to amphibole, and precipitation of hematite along the eclogite – carbonate rim. The average salinity from the group of inclusions in this sample was 10.5 wt.% NaCl. It is too few observed relationships between precipitated rutile together with measured inclusions to say anything about the relationships between titanium solubility and salinity in these veins. The only place where hematite are seen to be deposited are at the boundary with the kgr11 carbonate vein. This sample also show the lowest salinity measured. Salinity is important in the transport and complexation of metals in solution as Cl⁻ complexes (Seward et al., 2014). It is perhaps possible that the low salinity conditions at the interface in kgr11 caused Fe from the breakdown reaction of garnet to amphibole to immediately deposit at the boundary with the vein. And that this is only seen in this sample because of lower solubility of Fe in the vein because of lower salinity. With only one observation this is speculative and should be analyzed with more observations and more detailed analysis of carbonate fluid composition with for instance raman spectroscopy.

The origin and range of salinities in metamorphic fluids (including fluid inclusion recordings from eclogite) have been reviewed by Yardley et al., (2002). Eclogites and metabasites was found with salinities ranging from 2 wt.% to >30 wt.%. The authors compared the salinity of recorded fluids with the tectonic background of the rock body. They found that eclogites and metabasites originating from subducted oceanic lithosphere had fluid compositions with an overall lower salinity than those protoliths associated with continental crust. The average salinity of the Engebø eclogite fluids recorded in this thesis would plot in the same field as

recordings from high salinity, continental protolith rocks in the review after Yardley et al., (2002).

Yardley et al., (2002) argued that the high salinity fluids found in some continental eclogites could have been caused by the consumption of H₂O in metamorphic reactions. The residual metamorphic water would have an increase in wt.% NaCl when H₂O was removed.

Retrograde mineral assemblages observed at the Engebøfjellet eclogite are seen as garnet breakdown to amphibole. This reaction might have been important for increasing salinity of metamorphic fluids because it consumes H₂O.

6.4 Conditions of titanium solubility.

Rutile have been precipitated as large euhedrally shaped crystals in veins of mainly omphacite and quartz composition. Rutile tend to precipitate at the immediate boundary zone between a quartz vein and the eclogitic matrix . Rutile in veins often have large elongated euhedrally shaped omphacite crystals that sometimes are completely surrounded by rutile as mineral inclusions. The omphacite are believed to have been a product of fluid precipitation, this is because of the observation of large elongated crystals that seems to have grown uninterrupted at an angle from the vein-eclogite interface. This observation imply that rutile rich fluid also carries abundant omphacite ions in solution.

The solubility of TiO₂ in the presence of albite have been studied experimentally (Audetat et al., 2005). The solubility of TiO₂ in an 9 Wt.% albite solution, was up to one order of magnitude larger compared to the solubility of Ti in pure waters at similar pressure and temperature conditions. The solubility of Ti in a 15 wt.% NaCl solution was also determined experimentally by Audetat et al., (2005). The authors concluded that the solubility of Ti in the 15 wt.% NaCl solution increased solubility 2-3 times. This was caused by increased ionic potential of the solution, not Cl⁻ complexing with Ti. The study did not discuss the effect of other types of salt, for instance FeCl₂, on the solubility of Ti. Omphacite breakdown to albite in symplectite was observed in veins in this thesis. The presence of omphacite within rutile in veins indicate that rutile bearing fluid was rich in omphacite and possibly its breakdown constituents such as albite.

Two examples from sample kgr4C1 show the breakdown of pyrite to an iron oxide mineral (figs. 27 and 30). The process of pyrite breakdown involves the donation of H⁺ to the fluid

phase and thereby contributing to the H⁺ activity and lowering of the pH of the fluid. The pH of a solution has been suggested to increase titanium solubility at very low pH (Van Baalen et al., 1993).

A high pressure and temperature will increase the self-ionization of water (Seward et al., 2014). As mentioned, Audetat et al., (2005) argued that increased ionic potential of water increased the solubility of Ti. High temperature and pressure should therefore also contribute to the solubility of Ti in hydrothermal solutions.

Temperature, pressure, salinity, pH and content of dissolved albite could control the capability of fluids to transport Ti. The chemical factors could be diluted. Dilution of fluid is therefore proposed as a possible mechanism for the precipitation of rutile from a vein fluid.

6.5 Source of fluids

Stable isotopes.

Stable isotope analysis of carbonate minerals in eclogites and high-pressure rocks have previously been done by Agrinier et al., (1984) and Zhu et al., (2018) among others. The results from these workers was used because the data after the Agrinier study could be used to compare recordings from the same metamorphic region as Engebøfjellet (WGR). And the results after Zhu, could be used to compare the Engebøfjellet eclogite with eclogites from a different tectonic setting elsewhere in the world (Tianshan metamorphic belt, China).

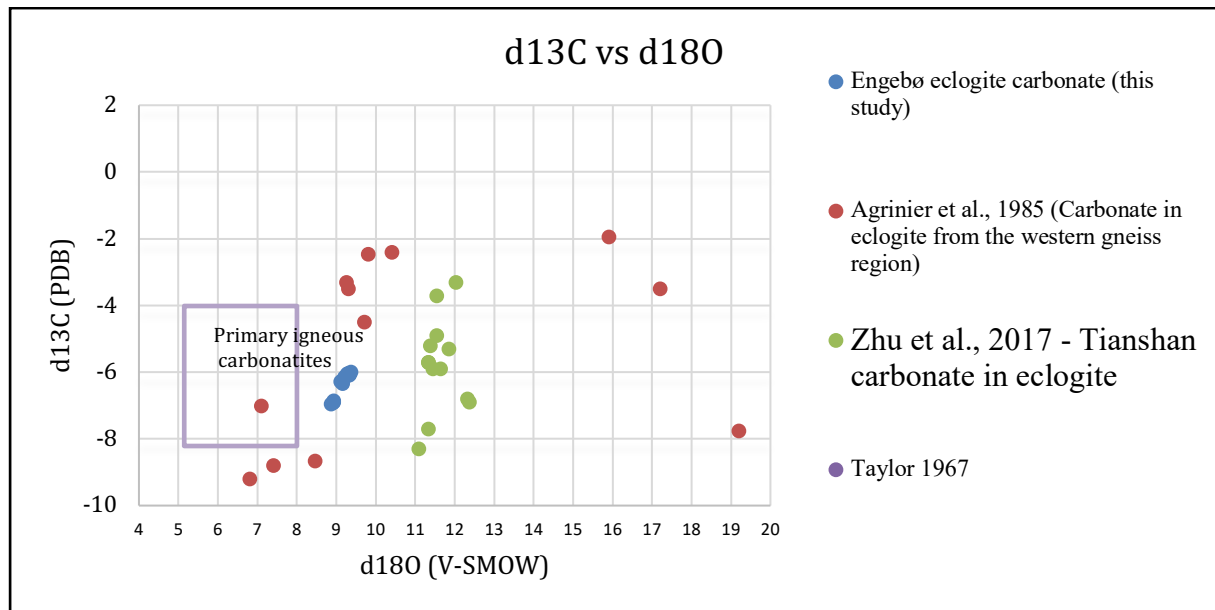


Figure 41. Comparison of isotope values of carbonate from veins in eclogite in western gneiss region, and one example from the Tianshan in China.

δ¹⁸O isotope values in eclogites have previously been reported from 3.5 to 12‰ (Javoy 1981);(Vidal et al., 1985). Meanwhile, the mantle δ¹⁸O isotopic signature range from mantle derived rocks range from 5.5-6‰ (Vidal et al., 1985). The field of primary igneous carbonatites after Taylor (1967) is shown in Fig.40.

The Engebø eclogites plot close to the isotopic composition of carbonate from veins in eclogite from other locations in the WGR fig.41, (Agrinier et al., 1985). Eclogites from the western gneiss region and the Tianshan eclogite (Zhu et al., 2017) plot within the previously reported 3.5-12‰ range of δ¹⁸O values in eclogite carbonate. The Tianshan eclogites was interpreted to have originated from a basaltic protolith that interacted with the sea floor prior to subduction and metamorphism. Interaction with a larger concentration of heavy δ¹⁸O isotopes from seawater could have caused a shift to the right in the eclogite carbonates from the Tianshan. If the Engebø eclogite have originated from a gabbroic source rock, this source rock has probably had less interaction with heavy δ¹⁸O rich fluids than an oceanic basalt would have.

A second possible explanation for the high salinity in fluid inclusion in the Engebøfjellet eclogite could be interaction from saline brines. Engebøfjellet is situated close to a major delamination structure that was active during the exhumation of the western gneiss region. The Nordfjord-Sogn detachment zone. This could have worked as a conduit for metamorphic

fluids. The magmatic signature of the vein- stable isotope data does not exclude interaction with external fluids of non-magmatic origin.

6.6 Suggestion for a model of rutile precipitation in eclogite veins.

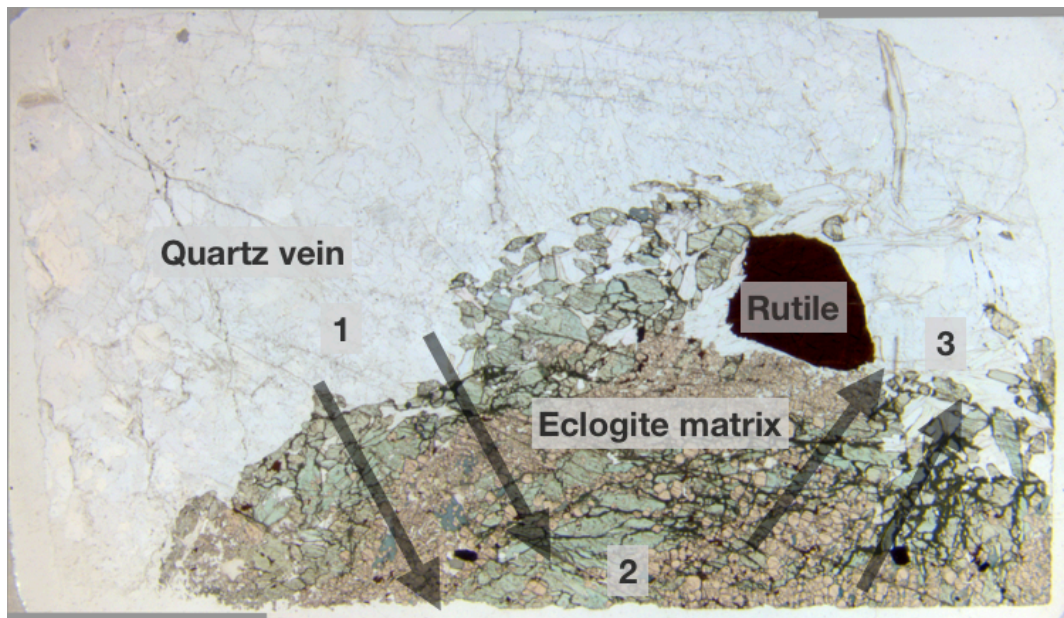


Figure 42. A suggestive model for rutile precipitation in veins.

This thesis have focused on the textures found at the interface between vein and eclogite matrix. (i.e sample kgr12, fig.42). It seems likely form textural relationships in several samples that there have been an interaction of fluids between these interfaces. A possible model for rutile precipitation are presented here based on fluid evolution at this interface.

Fluids with a relatively low salinity, pH and amount of dissolved albite species (Audetat et al., 2005) could enter the eclogite matrix and force its way along grain boundaries and cracks due to overpressure in the veins and fluid phase (Philippot et al., 1990). Such overpressures could exist during exhumation due to localized build ups of stress. H₂O in the fluid would be consumed by the garnet to amphibole transformation reaction, increasing the salinity of the residual fluid. Fe are released by this retrogression reaction (Kleppe 2013), and are consumed by the breakdown of pyrite to hematite, and rutile to ilmenite. The evolved fluid, with a higher salinity and lower pH would have an increased solubility for Ti. As the lithostatic pressure exceeds the fluid pressure, the fluid would be forced out of the eclogite and enters the vein where it initially came from. At the vein interface the fluid are diluted, causing a drop in Ti solubility and precipitation of rutile.

7 Suggestions for further studies.

- Combined fluid inclusion and microstructure study of the Engebøfjellet veins.
- Compare trace element composition of the Engebø and rocks in the gabbroic protoliths in the Flekke area, to gain a better understanding of the extent of trace element fractionation during metasomatism.
- A larger fluid inclusion study on rutile related quartz veins to try to better constrain the conditions of Ti mobilization in hydrothermal veins.

8 Conclusion.

- Primary fluid inclusions were found in quartz and carbonate vein material from the Engebø eclogite.
- Obtained eutectic temperatures suggest the NaCl-CaCl₂-H₂O composition of most of the analyzed fluid inclusions. The average salinity for the inclusions was 16.3 wt.% NaCl equ. Homogenization temperature were recorded in the interval from 150 to 450°C
- Rutile was usually deposited at vein-host rock contact, often with intergrowth of omphacite. The salinity of inclusions in one quartz vein associated with rutile phenocrystals was 12.5 wt.%.
- Calcite in veins show a magmatic $\delta^{13}\text{C}$ and $\delta^{18}\text{O}$ signature. Indicating that CO₂ in calcite was derived from a magmatic source.
- REE patterns of eclogite resembles normal MORB rather than OIB origin for the protolith.
- Eu anomaly in leuco-eclogite samples is used to support magmatic fractionation under low pressure conditions.

9 References

Activation laboratories, 2018.

Andersen, T., Burke, E.A.J. and Austrheim, H., 1989. Nitrogen-bearing, aqueous fluid inclusions in some eclogites from the Western Gneiss Region of the Norwegian Caledonides. *Contributions to Mineralogy and Petrology*, 103(2), pp.153-165.

Audéat, A. and Keppler, H., 2005. Solubility of rutile in subduction zone fluids, as determined by experiments in the hydrothermal diamond anvil cell. *Earth and Planetary Science Letters*, 232(3-4), pp.393-402.

Bakker, R.J., 1997. Clathrates: Computer programs to calculate fluid inclusion V-X properties using clathrate melting temperatures. *Computers & Geosciences*, v. 23, 1-18.

Bakker, R.J., 2003. Package FLUIDS 1. Computer programs for analysis of fluid inclusion data and for modelling bulk fluid properties. *Chemical Geology*, 194(1-3), pp.3-23.

Bakker, R.J., 2012. Can the vapour phase be neglected to estimate bulk salinity of halite bearing aqueous fluid inclusions?. *Central European Journal of Geosciences*, 4(2), pp.238-245.

Bodnar, R.J. and Vityk, M.O. (1994) Interpretation of Microthermometric Data for H₂O-NaCl Fluid Inclusions. In: De Vivo, B. and Frezzotti, M.L., Eds., *Fluid Inclusions in Minerals: Methods and Application*, Pontignosno-Siena, pp.117-130.

Bodnar, R.J., 2003a. Introduction to fluid inclusions. In I. Samson, A. Anderson, & D. Marshall, eds. *Fluid Inclusions: Analysis and Interpretation*. Mineral. Assoc. Canada, Short Course 32, 1-8

Bodnar, R.J., 2003b. Introduction to aqueous fluid systems. In I. Samson, A. Anderson, & D. Marshall, eds. *Fluid Inclusions: Analysis and Interpretation*. Mineral. Assoc. Canada, Short Course 32, 81-99.

Borisenko, A.S., 1977. Study of the salt composition of solutions in gas-liquid inclusions in minerals by the cryometric method. *Soviet Geol. Geophys.*, 18, pp.11-19.

Bozzo, A.T., Hsiao-Sheng, C., Kass, J.R. and Barduhn, A.J., 1975. The properties of the hydrates of chlorine and carbon dioxide. *Desalination*, 16(3), pp.303-320.

Diamond, L.W., 1992. Stability of CO₂ clathrate hydrate+ CO₂ liquid+ CO₂ vapour+ aqueous KCl-NaCl solutions: Experimental determination and application to salinity estimates of fluid inclusions*. *Geochimica et Cosmochimica Acta*, 56(1), pp.273-280.

Bozzo, A.T., Hsiao-Sheng, C., Kass, J.R. and Barduhn, A.J., 1975. The properties of the hydrates of chlorine and carbon dioxide. *Desalination*, 16(3), pp.303-320.

Bjørnerud, M.G., Austrheim, H. and Lund, M.G., 2002. Processes leading to eclogitization (densification) of subducted and tectonically buried crust. *Journal of Geophysical Research: Solid Earth*, 107(B10), pp.ETG-14.

Braathen, A. and Erambert, M., 2014. Structural and metamorphic history of the Engebøfjellet Eclogite and the exhumation of the Western Gneiss Region, Norway. *Norwegian Journal of Geology/Norsk Geologisk Forening*, 94(1).

- Coleman, R.G., Lee, D.E., Beatty, L.B. and Brannock, W.W., 1965. Eclogites and eclogites: their differences and similarities. *Geological Society of America Bulletin*, 76(5), pp.483-508.
- Cuthbert, S.J., Carswell, D.A., Krogh-Ravna, E.J. and Wain, A., 2000. Eclogites and eclogites in the Western Gneiss region, Norwegian Caledonides. *Lithos*, 52(1-4), pp.165-195.
- Duan, Z., Møller, N. and Weare, J.H., 1992a. An equation of state for the CH₄-CO₂-H₂O system: I. Pure systems from 0 to 1000 C and 0 to 8000 bar. *Geochimica et Cosmochimica Acta*, 56(7), pp.2605-2617.
- Duan, Z., Møller, N. and Weare, J.H., 1992b. An equation of state for the CH₄-CO₂-H₂O system: II. Mixtures from 50 to 1000 C and 0 to 1000 bar. *Geochimica et Cosmochimica Acta*, 56(7), pp.2619-2631.
- Duscsek, W., Kleinrahm, R. and Wagner, W., 1990. Measurement and correlation of the (pressure, density, temperature) relation of carbon dioxide II. Saturated-liquid and saturated-vapour densities and the vapour pressure along the entire coexistence curve. *The Journal of Chemical Thermodynamics*, 22(9), pp.841-864.
- Fall, A., Tattitch, B. and Bodnar, R.J., 2011. Combined microthermometric and Raman spectroscopic technique to determine the salinity of H₂O–CO₂–NaCl fluid inclusions based on clathrate melting. *Geochimica et Cosmochimica Acta*, 75(4), pp.951-964.
- Foreman, R., Andersen, T.B. and Wheeler, J., 2005. Eclogite-facies polyphase deformation of the Drøsdal eclogite, Western Gneiss Complex, Norway, and implications for exhumation. *Tectonophysics*, 398(1-2), pp.1-32.
- Gao, J., John, T., Klemd, R. and Xiong, X., 2007. Mobilization of Ti–Nb–Ta during subduction: evidence from rutile-bearing dehydration segregations and veins hosted in eclogite, Tianshan, NW China. *Geochimica et Cosmochimica Acta*, 71(20), pp.4974-4996.
- Gebauer, D., Lappin, M.A., Grünenfelder, M. and Wyttenbach, A., 1985. The age and origin of some Norwegian eclogites: A U-Pb zircon and REE study. *Chemical Geology: Isotope Geoscience section*, 52(2), pp.227-247.
- Griffin, W.L., Ahmed, N. and Perry Jr, E.C., 1982. Oxygen-isotope studies of some Norwegian eclogites. *Terra Cognita*, 2(3), pp.323-324.
- Hacker, B.R., 1996. Eclogite Formation and the Rheology, Buoyancy, Seismicity, and H₂O Content of Oceanic Crust. *GEOPHYSICAL MONOGRAPH-AMERICAN GEOPHYSICAL UNION*, 96, pp.337-346.
- Huang, H., Niu, Y., Zhao, Z., Hei, H. and Zhu, D., 2011. On the enigma of Nb-Ta and Zr-Hf fractionation—A critical review. *Journal of Earth Science*, 22(1), pp.52-66
- John, T. and Schenk, V., 2003. Partial eclogitisation of gabbroic rocks in a late Precambrian subduction zone (Zambia): prograde metamorphism triggered by fluid infiltration. *Contributions to Mineralogy and Petrology*, 146(2), pp.174-191.
- Jiang, S.Y., Wang, R.C., Xu, X.S. and Zhao, K.D., 2005. Mobility of high field strength elements (HFSE) in magmatic-, metamorphic-, and submarine-hydrothermal systems. *Physics and Chemistry of the Earth, Parts A/B/C*, 30(17-18), pp.1020-1029.
- Jin, Z.M., Zhang, J., Green, H.W. and Jin, S., 2001. Eclogite rheology: Implications for subducted lithosphere. *Geology*, 29(8), pp.667-670.
- Kleppe, S., 2013. *The Engebøfjellet Eclogite, Sunnfjord: petrology and modal analysis of a world class rutile-ore deposit* (Master's thesis).

- Korneliussen, A., McLimans, R., Braathen, A., Erambert, M., Lutro, O. and Ragnhildstveit, J., 2000. Rutile in eclogites as a mineral resource in the Sunnfjord region, western Norway. *Norges Geologiske Undersøkelse*, 436, pp.39-48
- Kylander-Clark, A.R.C., Hacker, B.R. and Mattinson, J.M., 2008. Slow exhumation of UHP terranes: titanite and rutile ages of the Western Gneiss Region, Norway. *Earth and Planetary Science Letters*, 272(3-4), pp.531-540.
- Zhang, Y.G. and Frantz, J.D., 1987. Determination of the homogenization temperatures and densities of supercritical fluids in the system NaCl-KCl-CaCl₂-H₂O using synthetic fluid inclusions. *Chemical Geology*, 64(3-4), pp.335-350.
- Liu, L.G., 1980. Phase relations in the system diopside-jadeite at high pressures and high temperatures. *Earth and Planetary Science Letters*, 47(3), pp.398-402.
- Liu, L., Xiao, Y., Aulbach, S., Li, D. and Hou, Z., 2014. Vanadium and niobium behavior in rutile as a function of oxygen fugacity: evidence from natural samples. *Contributions to Mineralogy and Petrology*, 167(6), p.1026.
- Luth, R.W., 1995. Experimental determination of the reaction dolomite + 2 coesite = diopside + 2 CO₂ to 6 GPa. *Contributions to Mineralogy and Petrology*, 122(1-2), pp.152-158
- Masterton, W.L., Hurley, C.N. and Neth, E.J., 2012. *Chemistry: principles and reactions*. Brooks/Cole Cengage Learning, pp.593.
- McKibben, M.A. and Barnes, H.L., 1986. Oxidation of pyrite in low temperature acidic solutions: Rate laws and surface textures. *Geochimica et Cosmochimica Acta*, 50(7), pp.1509-1520.
- McSween, H.Y., Richardson, S.M., Uhle, M.E. and Uhle, M., 2003. *Geochemistry: Pathways and processes*. (2edt) Columbia University Press.
- Miller, C., Zanetti, A., Thöni, M. and Konzett, J., 2007. Eclogitisation of gabbroic rocks: redistribution of trace elements and Zr in rutile thermometry in an Eo-Alpine subduction zone (Eastern Alps). *Chemical Geology*, 239(1-2), pp.96-123.
- Migdisov, A., Williams-Jones, A.E., Brugger, J. and Caporuscio, F.A., 2016. Hydrothermal transport, deposition, and fractionation of the REE: Experimental data and thermodynamic calculations. *Chemical Geology*, 439, pp.13-42.
- Philippot, P. and Selverstone, J., 1991. Trace-element-rich brines in eclogitic veins: implications for fluid composition and transport during subduction. *Contributions to Mineralogy and Petrology*, 106(4), pp.417-430.
- Robb, L., 2004. *Introduction to ore-forming processes*. Blackwell publishing
- Rudnick, R.L., Barth, M., Horn, I. and McDonough, W.F., 2000. Rutile-bearing refractory eclogites: missing link between continents and depleted mantle. *Science*, 287(5451), pp.278-281.
- Ryzhenko, B.N., Kovalenko, N.I. and Prisyagina, N.I., 2006. Titanium complexation in hydrothermal systems. *Geochemistry International*, 44(9), pp.879-895.
- Jamtveit, B., Bucher-Nurminen, K. and Austrheim, H., 1990. Fluid controlled eclogitization of granulites in deep crustal shear zones, Bergen arcs, Western Norway. *Contributions to Mineralogy and Petrology*, 104(2), pp.184-193.
- Javoy, M., 1971. Composition isotopique de l'oxygène dans les roches éclogitiques. *CR Acad. Sci. Paris*, 273, pp.2414-2417.

Jenkins, D., Brady, J (Accessed October 2018)

https://serc.carleton.edu/research_education/equilibria/other_diagrams.html

Seward, T.M., Williams-Jones, A.E. and Migdisov, A.A., 2013. The Chemistry of Metal Transport and Deposition by Ore-Forming Hydrothermal Fluids, Treatise on Geochemistry (Second Edition), pp. 29-57. Elsevier.

Shannon, R.D., 1976. Revised effective ionic radii and systematic studies of interatomic distances in halides and chalcogenides. *Acta crystallographica section A: crystal physics, diffraction, theoretical and general crystallography*, 32(5), pp.751-767.

Shepherd, T.J., Rankin, A.H. and Alderton, D.H., 1985. *A practical guide to fluid inclusion studies*. Blackie.

Steele-MacInnis, M., Lecumberri-Sanchez, P. and Bodnar, R.J., 2012. Short note: HokieFlinCs_H2O-NaCl: A Microsoft Excel spreadsheet for interpreting microthermometric data from fluid inclusions based on the PVTX properties of H2O-NaCl. *Computers & Geosciences*, 49, pp.334-337.

Sun, S.S. and McDonough, W.S., 1989. Chemical and isotopic systematics of oceanic basalts: implications for mantle composition and processes. *Geological Society, London, Special Publications*, 42(1), pp.313-345.

Vallis, F. and Scambelluri, M., 1996. Redistribution of high-pressure fluids during retrograde metamorphism of eclogite-facies rocks (Voltri Massif, Italian Western Alps). *Lithos*, 39(1-2), pp.81-92.

Van Baalen, M.R., 1993. Titanium mobility in metamorphic systems: a review. *Chemical Geology*, 110(1-3), pp.233-249.

Vidal, P. and Hunziker, J.C., 1985. Systematics and problems in isotope work on eclogites. *Chemical Geology: Isotope Geoscience section*, 52(2), pp.129-141.

Van Achterbergh, E., R. C.G., S.E. Jackson, and G. W.L., 2001. Data reduction software for LA-ICP-MS p. 239-243, in: S. P.), (Ed.), *Laser-Ablation-ICPMS in the Earth Sciences – Principles and applications*, Mineralogical Association of Canada short course series St John, Newfoundland.

Whitney, D.L. and Evans, B.W., 2010. Abbreviations for names of rock-forming minerals. *American mineralogist*, 95(1), pp.185-187.

Wood, S.A. and Samson, I.M., 1998. Solubility of ore minerals and complexation of ore metals in hydrothermal solutions. In *Reviews in Economic Geology* (pp. 33-80). Society of Economic Geologists.

Yardley, B.W.D. and Graham, J.T., 2002. The origins of salinity in metamorphic fluids. *Geofluids*, 2(4), pp.249-256.

Appendix

Fluid inclusion measurements.

Sample Id.	phase relation	Te	Tmice / Tm clath	Th	Th CO2 (V)
Sample 4D5 (2)-1		Quartz			
FIA3		H2O(L)+CO2(G)		(->L	
1	0,1		7,4	167	
2			9,3	175,5	
3		-38,6	8,4	187	
4		-42	7,3	172	
5			4,3	181	
FIA4		H2O(L)+CO2(G)		->L	
1	0,1		5,5	163	
2			5,6	164,5	
3			3,7	151	
4			9,5	154	
5			4,4	149	
6			7,3	155	
7			5,7	174	
8		-41	6,5	177	
9		-37,5	4,7	171	
FIA5		H2O(L)+CO2(G)		->L	
1	0,1		5,7	173,3	
2			7,2	149	
3			6	177	
4			5,5	159	
5		-33,5	5,3	167	
6		-38,5	4,4	169,5	
7		-40,5	4,7	175,5	
8			5,1	154,7	
Sample 4D5 (2)-2		Quartz			
FIA1	0,25	H2O(L)+CO2(G)		->L	
1		-35,5	0,8	183,5	
2			1,3	176,3	
3			0,7	179,4	
4		-37,3	0,7	185	
5		-34,5	0,1	177,5	
6		-41	1,7	187	
7		-34,7	1,3	184,5	

Sample Id.	phase relation	Te	Tmice / Tm clath	Th	Th CO2 (V)
FIA2		H2O(L)+CO2(G)		->L	
1	0,1		1,1	295	
2			1,3	291	
3			0,3	301,5	
4			0,2	301	
5			0,8	296,5	
6		-33,5	0,1	311	
7			-0,1	303	
8			1,2	365,5	
9			0	300,5	
10			0,1	307,3	
11			-0,2	296	
12			0,6	314,5	
13			0,5	296,5	
14			0,3	297,5	
15			0,9	306	
16			0,2	309	
17			1,3	321	
18		-35,7	0,2	343,3	
19			0,4	312	
20		-34,3	1,7	379	
21		-42,2	-0,1	334	
22			0,9	324	
23			1,2	319	
24			0,7	313,7	
25			-0,3	339	
FIA3		H2O(L)+CO2(G)		->L	
1	0,3		0,4	>400	
2			0,1	>400	
3			-0,7	>400	
4			-0,5	>400	
5		-40,7	0,3	>400	
6			0,9	>400	
7			-1,3	>400	
FIA4		H2O(L)+CO2(G)		->L	
1	0,25		0,8	326	
2			1,2	311	
3			0,9	321	
4			1,1	313	
5			1	317	
6			0,8	317	
7			1,2	340	
8			0,8	334	
9		-33,7	1,3	326	
10		-35,5	0,9	321,5	
11			1	357	

Sample Id.	phase relation	Te	Tmice / Tm clath	Th	Th CO2 (V)
Sample FI II.I		Calcite			
FIA4		H2O(L)+CO2(L)+CO2(G)		->L	
1	0,4		8,5	>400	
2			7,2	>400	
3			7	>400	
4			7,2	>400	
5			8,6	>400	
6		-56,2	8,9	>400	
7		-53,7	8,3	>400	
8			7,1	>400	
9			7,8	>400	
10		-53,5	7,3	>400	
FIA5		H2O(L)+CO2(L)+CO2(G)		->L	
1	0,35		4,7	>400	32,5
2		-56,5	6,2	>400	34
3			3,3	>400	35,3
4			4,2	>400	30,5
FIA6		H2O(L)+CO2(L)+CO2(G)		->L	
1	0,4		3,1	>400	33
2		-54,6	4,9	>400	29,5
3			2,7	>400	34,3
4			3,9	>400	31,5
5		-57,5	9,3	>400	32,1
6			6,2	>400	30,7
FIA7		H2O(L)+CO2(G)		->L	
1	0,15		1,8	269	
2			0,8	296	
3		-52	1,3	307	
4			1,1	295	
5			0,6	288	
6		-53,5	1,6	302	
7			0,9	289	
8			1,2	285	
FIA8	0,1	H2O(L)+CO2(G)		->L	
1			1,3	196	
2			1,7	191	
3			0,4	194	
4		-53	0,4	203	
5			0,1	186	
6			1,1	181	
7		-53,7	-0,2	201,5	
8			1,7	187	
9			1,5	199	

Sample Id.	phase relation	Te	Tmice / Tm clath	Th	Th CO2 (V)
FIA9	0,5	H2O(L)+CO2(L)+CO2(G)		->L	
1		-52,5		>400	34,5
2				>400	31,7
3		-53		>400	33,4
4				>400	34
5				>400	30,5
6				>400	33,5
7				>400	32
8				>400	29,5
9		-54		>400	35
FIA10	0,1	H2O(L)+CO2(G)		->L	
1			1,2	177	
2			0,5	175	
3			1,3	169	
4			1	174,5	
5			2,2	176	
6		-52,5	1,7	184,5	
7			0,1	177	
8			0,7	178	
9			0,3	175	
10			-0,3	169,5	
11		-54	1,3	183	
12			-0,1	173	
13			0,5	176,5	
14			0,8	182,5	
15			0,4	178	
FIA11	0,5			->L	
1		-51	8,5	>400	29,4
2			5,2	>400	32,3
3			5,9	>400	21
4		-48,8	7,4	>400	31,2
5			5,5	>400	30,7
6			9,1	>400	28,8
FIA12	0,25			->L	
1			-6,5	173	
2			-5,7	170	
3		-51,5	-9,3	196	
4			-7,3	187	
5			-5,9	172	
6			-8,7	207	
7		-53	-6,2	168	
8			-9,3	179	
9			-5,5	184	
10		-50,7	-8	189	
FIA13	0,25			->L	
1		-48,3	-5,9	163	
2			-8,1	171	
3			-6,9	180	
4		-48,6	-6,9	168	
5			-5,6	178	
6		-50	-6,4	184	
7		-49,6	-7,7	182	

Sample Id.	phase relation	Te	Tmice / Tm clath	Th
Sample 4D II				
FIA1		H2O(L)+CO2(G)		(->V)
1	0,3		2,4	418
2		-49,7	1,3	417
3		-51,5	4,7	429
4			1,5	422
5		-51	1,1	413
6			3,2	419
7			2,7	409
FIA2		H2O(L)+CO2(G)		->L
1	0,25		0,9	365
2		-50,7	1,3	376
3			2,1	357
4			0,6	362
5		-51,3	3,5	374
6			4,4	381
7			2,4	369
8			3,1	381
FIA3				->L
1	0,15	-52,7	-2,3	194
2	0,15		-0,5	179
3	0,15		-1,7	185
4	0,15		-2,3	191
5	0,25		-0,3	418
6	0,25		-2,7	428
7			0,3	387
8			-1	439
9		-49,5	1,1	412
10			-0,6	432
11			-2,1	405
12		-51,7	-2,7	436
13		-51,4	-1,4	393
14			-1,4	401
FIA4		H2O(L)+CO2(G)		->L
1	0,25	-54,6	0,6	342
2			1,1	327
3			2,4	318
4			-0,2	301
5			1,9	305
6		-53,7	1,6	311
	H2O(L)+CO2(G)+NaCl(s)			
FIA5			TmNaCl	Th
1			436	>450
2			232	393
3			406	>450
4			263	384
5			237	345
6			166	393
7			244	352
8			196,5	358
9			179	388
10			204	377
11			191	413
12			173,5	422
13			213	382
14			186	332

Sample Id.	phase relation	Te	Tmice / Tm clath	Th
FIA6	H2O(L)+CO2(G)+NaCl(s)			
1			312	>400
2			239	377
3			281	>400
4			206	>400
5			269	>400
6			103	376
7			184	392
8			312	>400
9			193	>400
10			331	>400
11			243	>400
12			229	>400
13			257	>400
14			187	359
15			136	>400
16			173	>400
17			235,6	387
18			238	>400
19			262	>400
20			168	364
21			273,3	>400
FIA7	H2O(L)+CO2(G)+NaCl(s)			
1			141	396
2			155	394
3			166,5	371
4			235	>400
5		-50,7	311,5	>400
6			286,5	>400
7			137	379
8			209	353
9			206,3	>400
10		-51,3	>400	>400
11			253	>400
12		-51,6	281	>400
13			179	>400
14			129	>400